THESIS FOR THE DEGREE OF LICENTIATE OF ENGINEERING

High Temperature Corrosion Behaviour of Ni-base Alloys and FeCrAl Alloys – The Influence of Water Vapour

Tommy Sand

Department of Chemistry and Chemical Engineering

CHALMERS UNIVERSITY OF TECHNOLOGY

Gothenburg, Sweden 2019

High Temperature Corrosion Behaviour of Ni-base Alloys and FeCrAl Alloys – The Influence of Water Vapour

Tommy Sand

Thesis for the degree of Licentiate of Engineering
Nr: 2019:16
Department of Chemistry and Chemical Engineering
Chalmers University of Technology
SE-412 96 Gothenburg
Sweden
Telephone + 46 (0)31-772 1000

Cover: *Top left;* Samples of Alloy 690 exposed for 200 hours in air/20 vol.% H_2O at 800 °C with different gas flow velocities. *Bottom left;* Plan-view SEM-SE image showing the interface between the 'darker area' labeled 1 and the 'brighter area' labeled 2. R*ight;* SEM-BSE images showing the oxide scale microstructures in the areas labeled 1 and 2.

Printed by Chalmers Reproservice

Gothenburg, Sweden 2019

Abstract

Electricity production, transportation, and manufacturing industry are some of the largest sources of greenhouse gas emissions. In many cases, these processes are carried out at high temperature and energy efficiency is limited by material degradation, so-called 'high-temperature corrosion'. Understanding material degradation at high temperature is of the utmost importance in making these processes more energy efficient, thereby reducing greenhouse gas emissions. One of the corrosive species at high temperature is water vapour, which is present in many industrial processes. Exposure of chromia-forming alloys in air that contains water vapour can result in the formation of volatile chromium-containing compounds from the chromia scale that protects the metal surfaces. This reduces the life times of the components and leads to the uncontrolled release of poisonous hexavalent chromium species. Strategies to mitigate the formation of volatile chromium-oxy-hydroxide species include: coating the metal surfaces; and adding alloying elements that promote the formation of an oxide scale that is less susceptible to the formation of volatile species. This thesis explores how Ni-base alloys and FeCrAl alloys, form oxide scales that exhibit low degrees of evaporation. The studies were carried out with a denuder technique to measure evaporation rates in the temperature range of 500-800 °C in an environment that consisted of air with 20-40 vol.% water. In-depth analyses of the formed oxide scales were performed using electron microscopy and X-ray techniques.

The studied Ni-base alloy contained approximately 30 wt.% chromium, 60 wt.% nickel, and 10 wt.% iron, and formed a chromium-rich oxide scale in the studied environments. Under the most severe condition, i.e., 800 °C and a high gas velocity, the initially very high evaporation rate decreased rapidly with exposure time. Examination of the oxide scale after 200 hours showed that an essentially chromium free and nickel-rich oxide had formed as a result of extensive chromium depletion in the oxide and near-surface region of the alloy. It is concluded that the formation of a Ni-rich cap layer drastically reduces the evaporation rate, which leads to the recovery of chromium levels in the near-surface region of the substrate, thereby allowing a new chromia layer to form at the metal/oxide interface. The final oxide scale was shown to be highly resistant to both evaporation and further oxidation.

One of the two studied FeCrAl alloys contained rather low concentrations of chromium (~12 wt.%) and aluminium (~4 wt.%), such that it had good structure stability, weldability, and formability. This alloy also contained about 1.3 wt.% silicon, to increase oxidation resistance. Under all the studied conditions (600-800 °C, dry and wet air), protective alumina scales were formed, showing very low levels of evaporation of chromium-oxy-hydroxides. From the exposure in wet air at 800 °C, a significantly high level of silicon was found in the oxide scale. GIXRD-measurements indicated the presence of mullite and tridymite in the scale.

The results described in thesis increase our knowledge of oxide formation on Ni-base alloys and FeCrAl alloys in wet air and can be used for guidance when selecting alloys in environments that cause the evaporation of chromium-oxy-hydroxides in the temperature range of 500-800 °C.

Keywords: High-temperature corrosion, Oxidation, Cr-evaporation, Ni-base alloy, FeCrAl alloy, Chromia scale, Alumina scale

List of publications

This thesis is based on the following papers:

Paper I

T. Sand, C. Geers, Y. Cao, J.E. Svensson, L.G. Johansson. Effective reduction of chromium-oxy-hydroxide evaporation from Ni-base Alloy 690, Oxidation of Metals, Volume 92, Issue 3-4, October 2019, Pages 259-279, ISSN 0030-770X, https://doi.org/10.1007/s11085-019-09935-9

Paper II

T. Sand, A. Edgren, C. Geers, V. Asokan, J. Eklund, T. Helander, J.E. Svensson, L.G. Johansson. Evidence for silicon affecting the high temperature corrosion behavior of FeCrAl alloys in humid air. Manuscript

Statement of authors' contributions

Paper I: I am the principal author. I performed all the experimental exposures and analyses using SEM and GIXRD. Yu Cao performed the XPS analyses.

Paper II: I am the principal author. I performed some of the experimental exposures and analyses using SEM and GIXRD. Aina Edgren performed most the experimental exposures and analyses using SEM and GIXRD. Vijayshankar Asokan performed the STEM analysis.

ACKNOWLEDGEMENTS

I would like to express my sincere gratitude to everyone who made this thesis possible and who helped me during this work.

I would like to thank my supervisors, Dr Christine Geers and Professor Jan-Erik Svensson, for the opportunity to carry out the work of this thesis at Chalmers University of Technology and for all their help and guidance along the way. I would like to thank Professor Lars-Gunnar Johansson for helping me to write articles and for teaching me more about chemistry. Thanks also to HTC, Vinnova, and Jernkontoret for support and funding, as well as the member companies Kanthal AB and PowerCell Sweden AB.

A big thank you to my Master's degree student Aina Edgren for all her great work.

Furthermore, I would like to thank the CMAL group for support with the microscopes, Yu Cao for the XPS-measurements, Vijayshankar Asokan for the STEM examinations, Vratislav Langer for help with the GIXRD, Sedi Bigdeli for computer simulations, Esa Väänänen and Torbjörn Jönsson for all their technical support, and the administration staff at OOMK.

I am deeply grateful to everyone who helped me in the lab, especially Patrik Alnegren, who helped me build my first system.

I also want to thank everyone at the Department of Environmental Inorganic Chemistry for creating and fostering a fun and open working environment.

Finally, I would like to thank my family and friends for their support.

CONTENTS

1 INTRODUCTION

Stainless steels and high-performance alloys are important materials in today's society. The yearly production volume of stainless steel is 50 million metric tonnes [1], and they are widely used in industrial applications and other areas, such as construction materials in bridges, household appliances etc. In fact, without stainless steels, our style of living would look very different. For example, stainless steel is required for the production of highly corrosive artificial fertilizers which increase the yield from crops by 3-4 times; and without these fertilizers a global population of 7 billion people would not be sustainable [2]. Moreover, electricity generation is heavily dependent upon stainless steels in, for example, nuclear power plants, power boilers, and concentrated solar power plants. The energy efficiencies of many of these processes are limited by the materials used in certain critical components. The development of new materials could help to increase the efficiencies of these processes, and consequently, reduce the carbon foot-print. Future applications also rely on the availability of high-performance materials. One example is the concept of a 'hydrogen society' in which hydrogen is used as the fuel for transportation and electricity/heat production. In a hydrogen society, fuel cells are used to convert the chemical energy into electrical energy and heat. Both the production of the fuel and the fuel cell itself require stainless steels, and material degradation is a major concern. These examples highlight the importance of developing new materials so that the processes can be made more energy efficient and the emissions of greenhouse gases can be reduced. This is especially relevant given that the largest sources of greenhouses gases are currently the above mentioned areas of application, i.e., electricity production, agriculture, transportation, residential heating, and manufacturing industries [3].

Many of the previously described processes operate at high temperatures and the utilised steels become degraded due to high-temperature corrosion. For the steel to be able to resist high-temperature corrosion, it is crucial that a protective, slow-growing and adherent oxide scale is formed on the metal surface. The type of oxide scale and how it forms depend on the composition of the alloy and the operating conditions, including the temperature and gas mixture used. Furthermore, the oxide scale is dynamic and can be broken down by changes in process conditions or depletion of the alloying elements in the metal. Stainless steels and Ni-base alloys are alloyed with chromium to be able to form a protective chromium rich oxide scale. In oxidising environments that contain water vapour, chromium-rich oxide scales are subject to degradation through the formation of volatile chromium-oxy-hydroxides [4]. Evaporation of these volatile species have detrimental effects on the metal (owing to the depletion of chromium) or on the process (through poisoning of critical components, such as catalysts). To prevent the formation of chromium-oxy-hydroxide, protection of the metal is essential. This can be accomplished by applying protective coatings or by selecting alloys that form protective scales that are less susceptible to evaporation. In both these instances, the purpose is to minimise the content of chromium in the outer part of the scale that is in direct contact with the environment, thereby reducing the evaporation of chromium-oxy-hydroxide.

This thesis explores how different alloy systems behave in air, that contains high concentrations of water within the temperature range of 500-800 °C. The alloy systems investigated range from an austenitic stainless steel (310S), and a Ni-base alloy (Alloy 690) to ferritic alumina-forming alloys (Alkrothal® 14 and Alloy 197). Both 310S and Alloy 690 form chromia scales during exposure at high temperature. The main difference between the two alloys is that 310S is iron-based while Alloy 690 is nickel-based. Since the evaporation of chromium-oxy-hydroxide releases chromium from the scale, the scale microstructure changes which can lead to the formation of wanted or un-wanted oxide phases. By varying the temperature and gas velocity, it is possible to influence the rate of evaporation of volatile species, such that the evolution of the scale microstructure can be studied. The ferritic alumina-forming alloys are FeCrAl alloys that contain a sufficient amount of aluminium to allow the formation of alumina scales. The chromium in these alloys is added for the so-called 'third-element effect' [5], whereby chromium facilitates the formation of an initial transient oxide scale that precedes the formation of a continuous alumina scale. For these alloys, the evaporation rates of chromium-oxy-hydroxide are expected to be low due to the low content of chromium in the outer part of the scale. However, during the initial transient stage, some

evaporation of chromium-oxy-hydroxide can occur. In the present study, time-resolved, quantitative studies of the evaporation rate are performed to gain insights into this mechanism, so that the implications for the final applications can be assessed. Another important aspect is that the slow formation of the alumina scale renders it difficult for the alloys to form protective alumina scales at the lowest temperature studied, i.e., 600 °C. The ability to form a protective scale can be improved by increasing the concentrations of aluminium and/or chromium in the alloy. However, this in turn leads to impaired weldability, formability and structure stability. Recently, it has been reported that the addition of relatively small amounts of silicon (1-2 wt.%) improves the ability to from protective scales with fewer detrimental effects on the other properties of the material [6]. In this study, an alloy with rather low levels of chromium (~12 wt.%) and aluminium (~4 wt.%) but with the addition of about 1.3 wt.% silicon has been examined, to determine its suitability within the investigated environment and temperature range.

The purpose of this thesis is to increase our current understanding of oxide formation and evolution in air that contains high concentrations of water vapour. Special emphasis is placed on studying the levels of chromium-compounds evaporated from the different scales. This knowledge can be used as guidance for material selection in applications that operate under conditions with wet air. Furthermore, the results can be used for designing new materials that exhibit minimal evaporation of the protective scale.

2 THEORY

2.1 PROCESSES WITH WET AIR

Many industrial applications involve processes that are conducted in air that contains water vapour, and at high temperature. In many cases, stainless steels and/or high-performance alloys are used as construction materials, e.g., in heat exchangers or in systems for the transportation of gases or other media. Figure 1 illustrates three of the most common processes in which the presence of water vapour and oxygen can result in the formation of volatile chromium-oxy-hydroxide, viz. in combustion, reforming, and fuel cells.

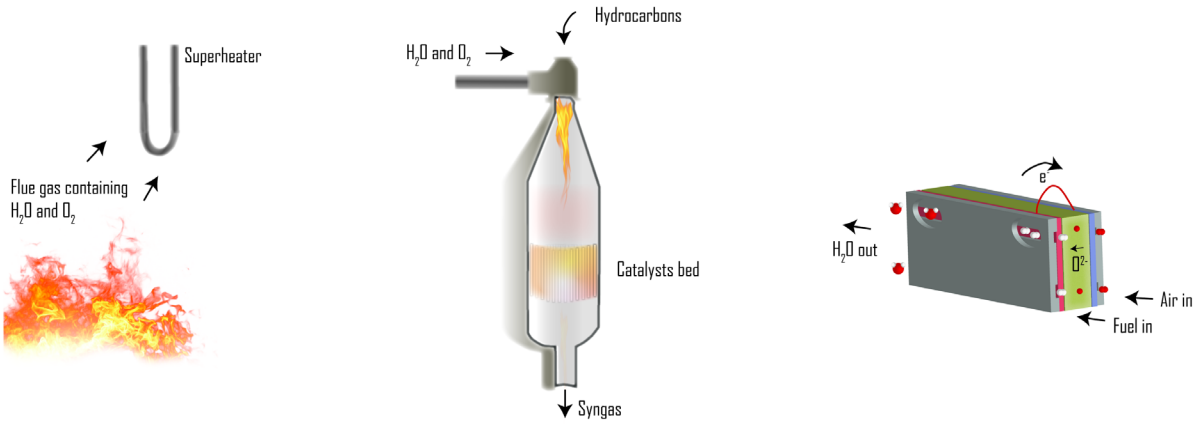

(a) Combustion (b) Reforming (c) Fuel cell

Figure 1 The principles underlying: (a) combustion, (b) reforming, and (c) fuel cells. All of these processes involve oxygen and water.

2.1.1 COMBUSTION

The combustion of any matter that comprises of hydrocarbons, such as coal, natural gas or biomass, generates H_2O according to Reaction 1, resulting in an oxygen- and water vapour-containing environment. It is important to ensure that the combustion process takes place in an environment that has an excess of oxygen, which means that oxygen is always present in the flue gas. In coal combustion, the water content is typically around 10 vol.%, and the temperature of the supercritical steam in the most advanced coal-fired power plants is about 700 °C [7]. The energy efficiency of the power plant can be improved by increasing the temperature of the steam. In this way, the carbon footprint can be reduced. Another way to reduce greenhouse gas emissions is to capture the formed carbon dioxide (CO_2) using Carbon Capture and Storage (CCS). Since combustion in air contributes to high levels of nitrogen, the CO_2 molecules become diluted in the flue gas. Therefore, combustion with CCS is preferably performed in pure oxygen, in a process termed 'oxy-fuel firing'. However, corrosiveness increases in oxy-fuel firing because the water content increases to >30 vol.% [7].

$$C_xH_y + zO_2 \rightarrow xCO_2 + \frac{y}{2}H_2O \qquad \text{Reaction 1}$$

During the combustion of biomass, the moisture content of the biomass contributes to an increase in the amount of water in the flue gas. Typically, the water content is about 20 vol.% and the temperature of the steam is kept at maximum 570 °C [8].

In the combustion of coal, water is not considered to be the most corrosive species in the process environment, since coal combustion results in corrosive gases such as SO_2/SO_3, leading to sulphidation [9]. The same applies to the combustion of biomass, which results in the deposition of alkali salts on steel surfaces, thereby accelerating corrosion through chromate formation [10]. Nonetheless, elucidating the role of water vapour and the formation of volatile chromium-oxy-hydroxides is important for the understanding of the overall corrosion process taking place in these process environments.

2.1.2 REFORMING

Reforming is a chemical process through which hydrocarbons such as methane or diesel are converted to syngas comprising mainly CO and H_2. This gas has a high value because it can be combusted to generate heat and electricity or converted to almost pure H_2 by applying the Water-Gas Shift (WGS) reaction, see Reaction 2 [11]. Steam reforming, in which the methane is mixed with water, is currently the most frequently used method for the production of hydrogen gas, which is used in the production of ammonia and for petroleum refining. Steam reforming is an endothermic reaction, requiring heat input from burners inside a firebox. If reforming is performed with a mixture of oxygen and water vapour the reaction will instead be exothermal and the reformer can be built in a more compact design; this technology is termed Auto Thermal Reforming (ATR), see Reaction 3 for the reformation of methane [11]. The major draw-back associated with this process is that the H_2:CO ratio is lower than for steam reforming, which entails a H_2:CO ratio closer to 3 [11]. Following reformation, the reformate gas, which is at a temperature >800 °C, needs to be cooled to <300 °C for the WGS reaction to take place. Heat exchange to recover the heat from the reformate gas is usually carried out to make the process more energy-efficient. This heat can be used to warm up the steam or steam/air mixture before it is mixed with the hydrocarbon and fed into the reformer. A gas mixture that consists of H_2O and O_2 in the heat exchanger would then generate an environment that can cause the formation of chromium-oxy-hydroxides. If these chromium-oxy-hydroxide enter the reformer they can inhibit the catalysts used in the reformation process.

$$CO + H_2O \rightarrow H_2 + CO_2 \qquad \text{Reaction 2}$$

$$4CH_4 + 2H_2O + O_2 \rightarrow 10H_2 + 4CO \qquad \text{Reaction 3}$$

2.1.3 FUEL CELLS

Fuel cells are electro-chemical devices that convert chemical energy to electricity and heat. The underlying principle of fuel cells is that a fuel, e.g., H_2 is fed into one side of an electrolyte and air is fed into other side. Ion movement through the electrolyte then leads to the transport of electrons through an external circuit, creating an electrical current. The overall reaction results in the formation of water, see Reaction 4. There are different types of fuel cells, including Proton Exchange Membrane (PEM) fuel cells and Solid Oxide Fuel Cells (SOFCs). In PEM fuel cells, hydrogen is required as the fuel and the operating temperature is usually <100 °C [12]. In SOFCs, different fuels, e.g., hydrogen or methane, can be used owing to the higher operating temperatures, which are typically in the range of 600-1000 °C [13]. The air side of a SOFC contains air at ambient humidity (up to 3 vol.% H_2O), an environment that promotes the formation of chromium-oxy-hydroxides from metallic components, such as the interconnects [14]. The formation of these chromium-containing species can result in so-called 'cathode poisoning' [15], as well as excessive degradation of metallic components.

Fuel cells require surrounding components, for handling heat exchanging etc. These Balance-of-Plant (BoP) components may also be exposed to environments that contain high concentrations of H_2O and O_2, resulting in severe volatilisation of chromium-oxy-hydroxides [16].

$$\frac{1}{2}O_2 + H_2 \rightarrow H_2O \qquad \text{Reaction 4}$$

2.2 FUNDAMENTAL OXIDATION

2.2.1 METAL OXIDATION

Metals that are subjected to a non-inert environment will in some way interact with that environment resulting in chemical reactions that make the metal more or less fit-for-purpose with respect to the intended application. In air, most metals (with the exceptions of gold, silver and platinum) react with oxygen, forming metal oxides according to Reaction 5 [17]. The structure and properties of the oxide depend on different factors, such as the type of metal, environment, temperature, pressure, and time. Once the oxide is formed, a barrier exists between the metal and the environment and further reactions require transport of reactants through this barrier. At elevated temperatures, this oxide is commonly referred to as an oxide scale. The formation of the initial oxide

scale can in a simplistic way be described in terms of three steps [17], as illustrated in Figure 2. The first step involves the adsorption of oxygen to the metal, the second step entails nucleation and growth of the oxide, and the third and final step is scale growth.

$$aM + \frac{b}{2}O_2 \rightleftarrows M_aO_b \qquad \text{Reaction 5}$$

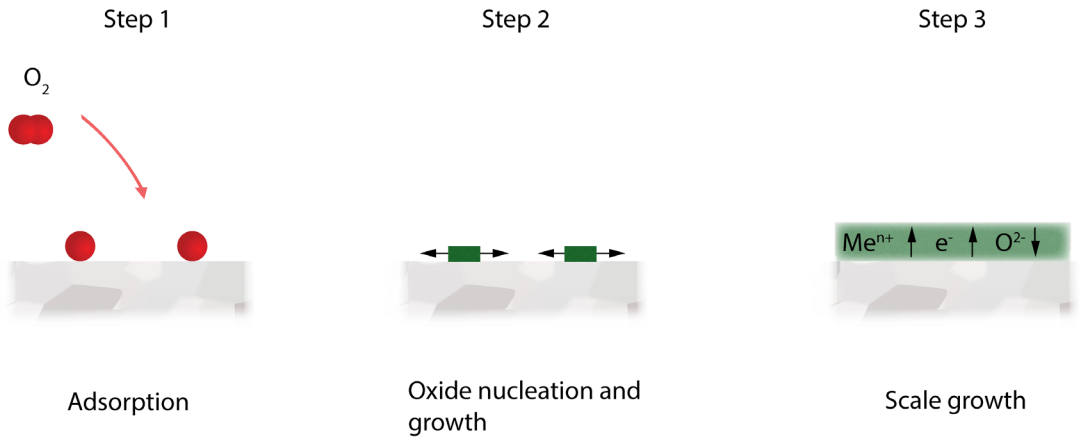

Figure 2 Schematic showing the formation of an oxide scale. Step 1, adsorption of oxygen; Step 2 oxide nucleation and growth; and Step 3, scale growth. Adapted from [17].

2.2.2 THERMODYNAMICS

Whether or not a metal oxide can form depends on the temperature and oxygen partial pressure in the environment. From the reaction for the formation of the metal oxide (Reaction 5), it is clear that the metal oxide can form and that the metal oxide can dissociate to a metal depending on the oxygen partial pressure. The Gibbs free energy of a system at constant temperature and pressure is defined according to Equation 1:

$$G = H - T \cdot S \qquad \text{Equation 1}$$

where G is Gibbs free energy, H is enthalpy, T is temperature and S is entropy [18].

The Gibbs free energy can be used to determine whether or not a reaction is spontaneous. In order for the reaction to be spontaneous, the change in Gibbs free energy has to be <0. The Gibbs free energy for Reaction 5 is expressed by Equation 2:

$$\Delta G = \Delta G^0 + RTlnK_{eq} = \Delta G^0 + RTln\frac{a_{(M_aO_b)^{(s)}}}{a_{M(s)}^{a}a_{O_2(g)}^{\frac{b}{2}}} \qquad \text{Equation 2}$$

where ΔG^0 is the standard Gibbs free energy, R is the universal gas constant and K_{eq} is the equilibrium constant for the reaction, and a is the activity of corresponding reactants.

Since the activity (a) of solid substances is 1, the only two variables are the temperature and the activity of oxygen, which can be conveniently presented in a so-called Ellingham/Richardson-diagram, see Figure 3. From this diagram, it is possible to determine the oxygen partial pressure above which a metal oxide is thermodynamically stable, the so-called 'dissociation pressure'. Below the dissociation pressure, the metal oxide is not stable and any metal oxide will decompose to the pure metal and oxygen with time.

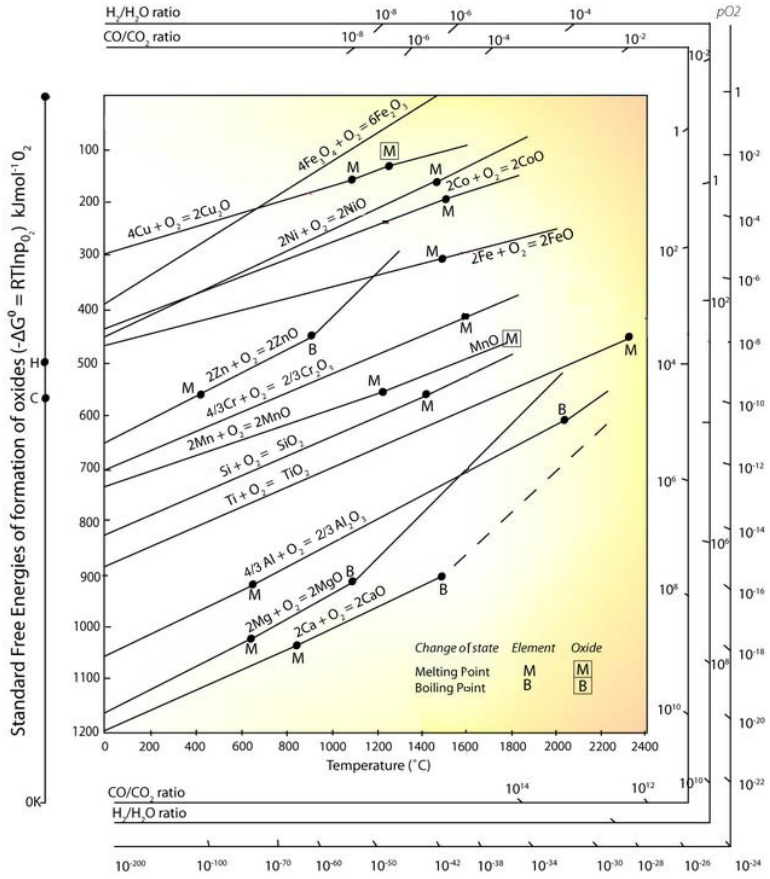

Figure 3 Ellingham/Richardson diagram for some of the most common metals/metal oxides [19].

2.2.3 KINETICS

The rate with which an oxide scale grows depends on various factors, such as solid-state diffusion through the scale, redox-reactions of the reactants, and scale properties. When diffusion through the scale is rapid, the growth rate is determined by the slowest redox-reaction in the system, which usually is the reactions at the gas/oxide interface [20]. In this case, the scale grows at a linear rate and can be described by Equation 3:

$$x = k_l t \qquad \text{Equation 3}$$

where x is the scale thickness, t is time and k_l the linear rate constant. This phenomenon is typically observed in cases with extremely thin scales, as well as in cases with porous and defect-rich scales.

If scale growth is governed by solid-state diffusion through the scale, the flux of ions/molecules/electrons needs to be considered. A model to describe this was first presented by Wagner [21], who used Fick's first law together with electron diffusion mechanisms to explain how an oxide scale grows at a parabolic rate. In principle, the model describes how gradients of oxygen partial pressure across the scale, together with the change in free energy for the metal oxide formation generate a driving energy for the ions to 'jump' between defects in the lattice, such that the metal oxide can form. The thicker the scale grows, the lower the driving energy becomes and the growth rate decreases. This is an ideal model and requires that certain criteria are met, such as thermodynamic equilibrium at the interfaces and inside the scale, steady-state conditions at the interfaces, as well as homogeneity of the phases. Nevertheless, the model is even today widely used to explain the growth of an oxide scale in a diffusion-controlled manner. The parabolic growth rate is described by Equation 4:

$$x^2 = K_p t + C \qquad \text{Equation 4}$$

where K_p is the parabolic rate constant and C is the integration constant.

The growth rate of an oxide can also follow a sub-parabolic pattern. This is usually observed for very thin oxides and has been explained in terms of electron channelling or the presence of cavities in the thin film [17].

In reality, an oxide scale is complex and non-static. This means that the diffusion mechanisms change over time, and this is especially true for complex alloy systems that contain multiple alloying elements that oxidises. The partial pressure changes locally within the scale and the activity of the alloying element in the alloy decreases or increases over time.

2.2.3.1 'Break-away' oxidation

'Break-away' oxidation is a mechanism whereby the oxidation is initially parabolic but following break-down of the oxide scale, a fast linear oxidation behaviour emerges. Most commonly, this is attributed to severe chromium depletion of the oxide and metal, leading to break-down of the protective chromium rich oxide [22, 23]. When the protective oxide scale is lost, rapid oxidation of iron-oxides occurs, leading to a drastic increase in the oxidation rate. Depletion of chromium can also occur in Ni-base alloys, with the consequence that nickel starts to oxidise. However, this will not trigger a linear rate of oxidation and is not termed 'break-away' oxidation. Huczkowski et al. [24] have instead labelled this as 'critical Cr-depletion'.

2.2.4 Oxide structure

The oxides formed on metals generally have a polycrystalline structure, even though amorphous and vitreous oxides also exist [17]. The structure of the oxide can be either stoichiometric or non-stoichiometric depending on the elements present in the oxide and the conditions under which it is formed. Highly stoichiometric oxides, such as α-Al_2O_3, still contain defects in the lattice, albeit to a lesser extent compared to non-stoichiometric oxides. In stoichiometric oxides, there are two common types of defects; Schottky and Frenkel defects. A Schottky defect entails incorporation of vacancies into the lattice, where both a cation and an anion are missing. A Frenkel defect involves the incorporation of a cation interstitial ion, which is balanced by a cation vacancy. The presence of these defects enables vacancy and interstitial movements in the lattice, at the same time as the stoichiometry and electron neutrality are maintained. Non-stoichiometric structures, e.g., Cr_2O_3, FeO, and Fe_2O_3, have chemical compositions that deviate from stoichiometry through either oxygen excess/deficiency or metal excess/deficiency [25]. On the one hand, if the oxide has an oxygen excess or metal deficit, the major defects present in the lattice will be oxygen interstitials or metal vacancies, respectively. This type of oxide is classified as a p-type semiconductor. On the other hand, if the oxide has either an oxygen deficiency or metal excess the predominant defects will be oxygen vacancies or metal interstitial, respectively. These types of oxides behave as n-type semiconductors. In non-stoichiometric oxides, the electro-neutrality is maintained by either extra electrons or electron holes. The nature and extent of the defects in the oxide influence how ions are transported through the scale, which in turn determines how the oxide scale grows. This is illustrated in Figure 4, where it can be seen that an n-type oxide with metal excess and a p-type oxide with metal deficiency grow at the gas/oxide interface, whereas an n-type oxide with oxygen excess and a p-type oxide with oxygen deficiency grow at the metal/oxide interface. It should be noted that the above description represents a model system. In reality, the complexity of the oxides is greater and mixtures of different structures create scales that grow at both the gas/oxide interface and the metal/oxide interface.

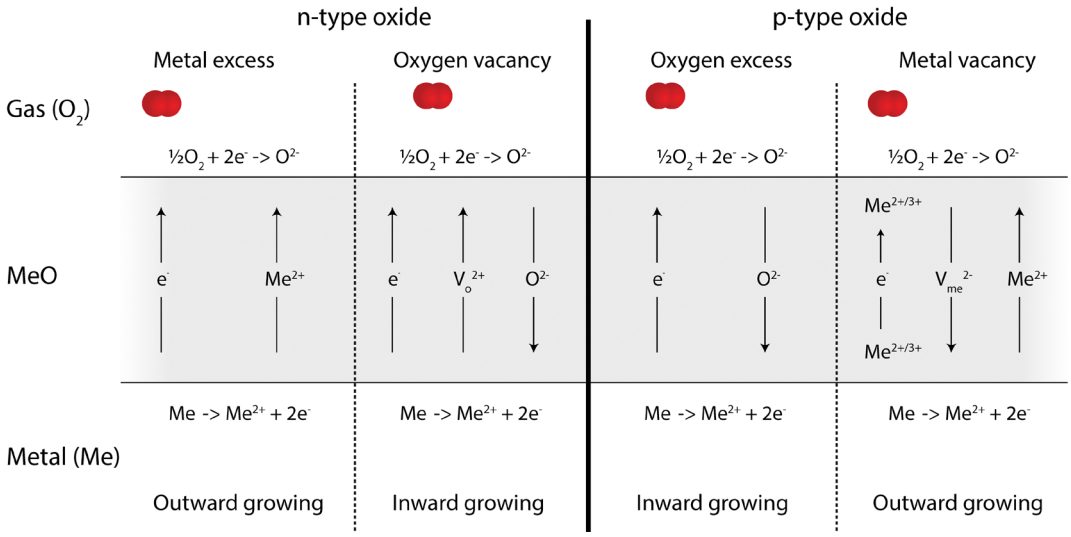

Figure 4 Illustration of the ionic diffusion patterns in n-type and p-type oxides and the growth directions of the oxide scale. Adapted from [26].

So far, the structures of the oxides have been discussed only on an elementary level. There are also microscopic and macroscopic features that influence the properties of an oxide scale. Since the oxide is polycrystalline, there are grain boundaries present in the scale that lead to short-circuit diffusion pathways through the scale [27]. The oxide grains are not static during high-temperature exposure and can grow and recrystallise with time. For an oxide scale to be protective, it needs to be dense, adherent and continuous. If the oxide is porous, cracked or has other macroscopic defects, ions and molecules can easily penetrate the scale [20]. Factors that cause these defects are stresses in the oxide, contaminants in the metal, and a too-fast growing scale, to mention a few examples.

Alloys can form different types of oxide structures depending on the alloy composition, temperature etc. The main oxide structures observed in this thesis are summarised below, and the structures are depicted in Figure 5.

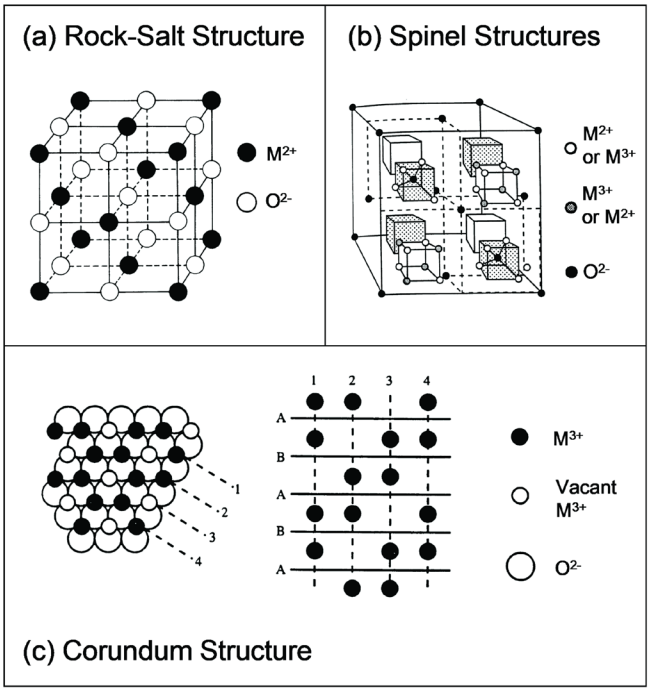

Figure 5 Crystalline structures of the most common oxide phases observed in this thesis: (a) rock-salt structure; (b) spinel structure; and (c) corundum structure [26].

2.2.4.1 Cr_2O_3

The vast majority of high-temperature alloys used at temperatures above approximately 600 °C rely on the formation of a chromia scale. The chromia scale has a corundum structure (see Figure 5c) in which the oxygen ions are packed in a hexagonally closed-packed structure, with the chromium ions occupying the octahedral holes in the lattice [28]. The chromia scale has a high degree of stoichiometry and superior protective properties compared to any iron-oxide. If the scale is formed on a Fe-base alloy it is possible that the formed scale is not pure Cr_2O_3 but rather consists of a mixture of Cr_2O_3 and Fe_2O_3, as the similarities shared by the different oxides make them completely soluble with each other [29].

It has been observed that the oxygen partial pressure influences which defects that are present in a Cr_2O_3-oxide. At low oxygen partial pressures, the oxide behaves as an n-type semiconductor, whereas at high oxygen partial pressures it behaves as a p-type semiconductor [30-32].

2.2.4.2 M_3O_4

Spinel oxides consist of metallic ions, such as $Fe^{2+,3+}$, $Mn^{2+,3+}$, Ni^{2+} and Cr^{3+}, which occupy the tetrahedral and octahedral sites in a cubic closed-packed crystal structure, see Figure 5b. A spinel oxide is either classified as: 'normal' when the M^{3+} occupies half of the octahedral sites and M^{2+} occupies every eighth tetrahedral site, or 'inverse' when every eighth tetrahedral site is occupied with an M^{3+} and the octahedral sites are split between M^{2+} and M^{3+}, e.g., Fe_3O_4 [17]. In general, spinel oxides are poorly protective, although the diffusion rate in the spinel depends on the elemental composition of the spinel.

2.2.4.3 NiO

NiO has the halite or rock-salt structure (NaCl) in which oxygen ions lie in a cubic close-packed structure, with the Ni-ions in octahedral interstitials, see Figure 5a [17]. NiO has a low level of stoichiometry and, consequently, is poorly protective owing to rapid diffusion through the oxide. It should be noted that the reaction between NiO and Cr_2O_3 to form $NiCr_2O_4$ occurs spontaneously [33].

2.2.4.4 Al_2O_3

α-Al_2O_3 has a corundum structure similar to that of Cr_2O_3, with hexagonally closed-packed oxygen ions and aluminium ions occupying the octahedral holes in the lattice [17]. However, α-Al_2O_3 is more stoichiometric resulting in a very low level of ion diffusivity, making it highly protective. The inward diffusion of oxygen through short-circuit grain boundaries is the main contribution of ion diffusion across an α-alumina [34] [35]. The growth kinetics is usually sub-parabolic, and at the high temperatures where grain coarsening occurs a decrease in the oxidation rate is observed due to grain growth [36]. Since the nucleation of α-alumina is rather slow, different, transient Al_2O_3 phases are normally formed at temperatures <1000 °C [37]. These transient alumina phases are metastable and transform to α-Al_2O_3 given sufficient time and appropriate temperature. The transient alumina phases, i.e., γ-alumina, θ-alumina, δ-alumina, and κ-alumina, are not as stoichiometric as α-alumina, and consequently exhibit faster growth rates. It has been observed in previous studies that these transient alumina phases grows outwards by metallic cation diffusion [38].

2.2.4.5 Mullite

Mullite is a crystalline structure with the composition $Al_2(Al_{2+2x}Si_{2-2x})O_{10-x}$, where x=0.25 results in stoichiometric mullite with formula $3Al_2O_3{\cdot}2SiO_2$ and x=0.40 gives $2Al_2O_3{\cdot}SiO_2$ [39]. Pure mullite is used in various high-temperature applications such, as refractory.

2.3 Corrosion by water vapour

Water vapour is a corrosive species at high temperatures. The effects of water vapour have been studied extensively over the years, and mechanisms that involve chromium evaporation and increased oxidation rates in environments at low oxygen partial pressures have been studied [4] [40-45]. Since water vapour is present in

many industrial processes, such as those previously presented in Section 2.1, an improved understanding of how water vapour influences corrosion is of the utmost importance.

2.3.1 Chromium evaporation

When a chromium-rich oxide is in contact with an environment that contains O_2 or O_2/H_2O at high temperatures, chemical reactions occur, resulting in the formation of gaseous species, see Figure 6. This is commonly referred to as 'chromium evaporation' and it depends on various factors, such as the temperature, the partial pressures of O_2 and H_2O, the gas velocities, and the scale structure. Examples of reactions that can occur are Reaction 6 and Reaction 7. Theoretical and experimental evaluations have been performed to determine the partial pressures of CrO_3 and $CrO_2(OH)_2$ over Cr_2O_3 at different temperatures [46, 47]. From these results, it can be concluded that at temperatures <900 °C, the main volatile compound is $CrO_2(OH)_2$. At temperatures <800 °C, the amount of CrO_3 is negligible.

$$Cr_2O_3(s) + 1.5\ O_2 = 2CrO_3(g) \qquad \text{Reaction 6}$$

$$Cr_2O_3(s) + 2H_2O + 1.5\ O_2 = 2CrO_2(OH)_2(g) \qquad \text{Reaction 7}$$

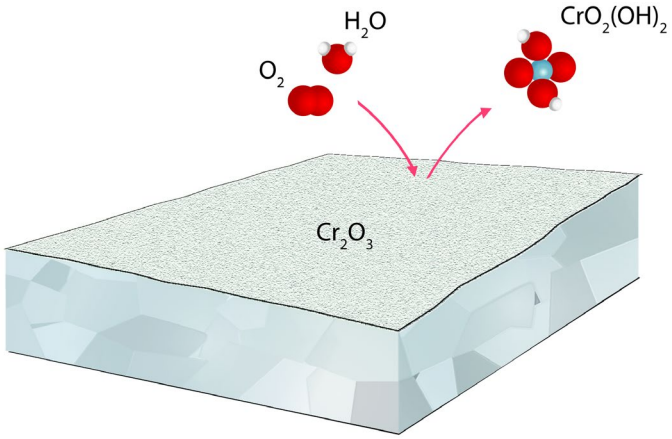

Figure 6 Schematic showing the principle of chromium evaporation. Water vapour and oxygen react with the chromia scale to form chromium-oxy-hydroxide.

The formation of $CrO_2(OH)_2$ from a chromia scale involves the oxidation of chromium (III) to the hexavalent state by O_2 followed by the hydrolysis of the Cr(III)-O-Cr(VI) bonds by H_2O [48]. Since an activation enthalpy is necessary for the evaporation reaction to occur, it is obvious that increasing the temperature will increase evaporation. Falk-Windisch et al. [14] have shown that when a temperature increase of 100 °C was implemented in the interval of 650-850 °C the evaporation rate increases by a factor of 2-3.

Increasing the partial pressures of H_2O and O_2 increases the evaporation rate, since Reaction 7 is pushed towards the formation of $CrO_2(OH)_2$. The maximum rate of evaporation in an environment that contains H_2O and O_2 occurs when the fraction of water is 0.57 and the fraction of oxygen is 0.43.

Since the saturation partial pressure of $CrO_2(OH)_2$ is low, equilibrium is quickly reached in a stagnant gas. However, in flowing gas streams, $CrO_2(OH)_2$ molecules are transported away from the reaction surfaces, thereby increasing the evaporation rate proportional to the gas velocity. The increase in evaporation rate due to increasing flow rates is valid up to a certain level, after which the evaporation rate instead depends only on the forward reaction expressed in Reaction 7. It has been shown by Froitzheim et al. [49] that in air with 3 vol.% H_2O, flow independency is reached at about 0.25 m/s. However, in another study, an increased rate of evaporation when the flow velocity was increased from 0.7 m/s to 6 m/s in air with 6 vol.% H_2O [24].

2.3.1.1 TEDMON KINETICS

Evaporation and oxidation are reactions that occur simultaneously during exposure at high temperatures in O_2/H_2O-environments. The evaporation reduces the scale thickness, while oxidation increases it. Tedmon [50] has proposed a model in which, at some elapsed exposure time, the rate of oxide growth becomes equal to the rate of evaporation. When this happens a constant oxide thickness is achieved. This can be described by Equation 5, where K_d is the oxide growth rate constant and k_s is the reduction of thickness constant. By setting the scale growth to zero, the critical scale thickness can be calculated using Equation 6. This model can also be applied for gravimetric data, resulting in a net mass change that is described as paralinear due to the parabolic oxide growth and the linear evaporation rate, as illustrated in Figure 7 [51].

$$\frac{dx}{dt} = \frac{K_d}{x} - k_s \qquad \text{Equation 5}$$

$$x = \frac{K_d}{K_s} \qquad \text{Equation 6}$$

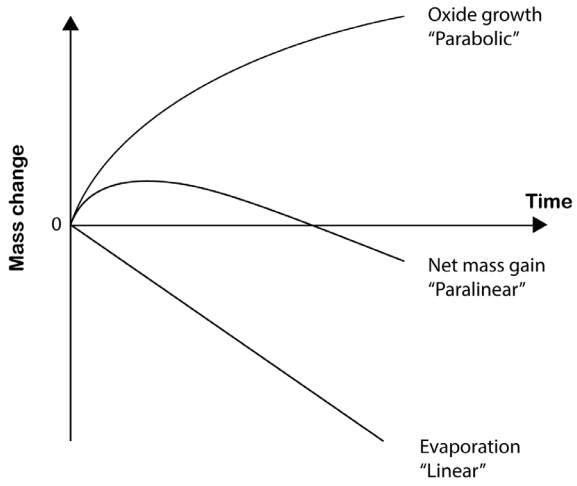

Figure 7 Schematic illustration showing a paralinear behaviour due to parabolic oxide growth and linear evaporation.

2.3.1.2 MITIGATING CHROMIUM EVAPORATION

The amount of volatile chromium-oxy-hydroxide formed can be reduced by applying various measures. One way to mitigate evaporation is to alloy with elements that form oxide scales with less amounts of chromium in the outer part. An alloying element that has been used widely for this purpose is manganese [14] [52]. The manganese promotes an outer layer of $(Cr,Mn)_3O_4$, which decreases the amount of chromium that is in contact with the environment, such that the evaporation rates are reduced 2-3 times [53]. The use of alloys that contain sufficient amounts of aluminium to allow an alumina scale to be formed is another way to add an alloying element to reduce chromium evaporation, (described in detail in Section 2.3.3.) A common approach to mitigating Cr-evaporation is to apply coatings to the steel surfaces separating the chromium-rich oxide scale from the environment. Examination of substrates coated with cobalt to form $(Co,Mn,Fe)_3O_4$ have revealed significantly reduced Cr-evaporation [54] [55]. Furthermore, nickel has been tested as a coating material at 800 °C, reducing the evaporation by 99% [56].

2.3.2 WATER VAPOUR AT LOW OXYGEN PARTIAL PRESSURES

In environments that contain H_2O but no O_2, there is no evaporation of chromium-oxy-hydroxide. However, in these environments, water is the oxidant and the nature of the oxidation is different from that when oxygen is the main oxidant [45]. Some proposed mechanisms for oxidation by water are increased diffusivity/solubility of oxygen in the metal [57], and the presence of so-called 'H_2/H_2O-bridges' in the voids in the oxide scale [58]. Henry

et al. [59] have suggested that the smaller ionic radius of OH^- compared to that of O^{2-} explains the faster oxide growth in these environments.

2.3.3 Water vapour effects on alumina

Water vapour also influences the formation and growth of alumina scales. Evaporation of Al_2O_3 by water vapour occurs according to Reaction 8. However, as the activity of this reaction is considered to be negligible at temperatures <1300 °C, it is not considered the be important at normal operating temperatures [60].

$$\frac{1}{2}Al_2O_3(s) + \frac{3}{2}H_2O(g) = Al(OH)_2(g) \qquad \text{Reaction 8}$$

FeCrAl alloys form transient oxides that contain chromium during the early stage of oxidation. The chromium in this oxide could be subject to the formation of chromium-oxy-hydroxides. Previous studies have shown that the evaporation from FeCrAl alloys is about 1-3 orders of magnitude lower than that from chromia scales at temperatures in the range of 800-1000 °C [61] [62]. After prolonged exposure time at high temperature, the amount of chromium in the outer part of the oxide scale should be very low, and the evaporation of chromium-oxy-hydroxide should be minimal.

Water vapour influences the structure of the alumina scale. It has been observed that the oxidation rate is higher in wet air compared to dry air [63]. This has been attributed to that water vapour stabilises γ-alumina which grows faster compared to α-alumina [38].

2.4 High-temperature resistant alloys

Steels are alloys that consist of iron and carbon. For the steel to be denoted as a stainless steel, a chromium content >10.5 wt.% is needed [64]. Other types of alloys are also used in high-temperature applications, for example Ni-base alloys, where the base of the composition is nickel rather than iron. Stainless steels and Ni-base alloys are construction materials that are often used at elevated temperatures for various purposes, such as heat exchanging, transportation of media, and the separation of media. The desired properties of these metallic alloys include: formability, weldability, good heat transfer, high strength, ductility, corrosion resistance, and relatively low prices. High-temperature alloys can be classified according to alloy composition, properties, and structure into the following families: carbon steels; low-alloyed steels; (austenitic, ferritic, martensitic) stainless steels; Ni-base alloys; Co-base alloys; alumina-forming ferritic alloys; and alumina-forming austenitic alloys. The families used in this thesis are described in more details below.

2.4.1 Austenitic stainless steels

Austenitic stainless steels are iron-based alloys that are stabilised with nickel to make them austenitic. In some instances, other austenite-stabilising elements such as manganese and nitrogen, are added to reduce cost. The high-temperature corrosion resistance of the steel is improved by increasing the chromium content and/or by adding silicon or Reactive Elements (REs), as in the case of 253MA™. Some of the most commonly used austenitic stainless steels for high-temperature service are presented in Figure 8. It should be noted that most of these alloys exist in different versions, with variations mostly related to the carbon content and grain size. For example, 304L (a low carbon-containing version of 304), more resistant against certain corrosion mechanisms, such as intergranular corrosion due to sensitisation. The high-temperature version of 304 is called 304H and it has large grains that increase creep strength. The two grades, 347 and 321, are stabilised with niobium or titanium, respectively, to avoid Cr-carbide precipitation, making them more resistant to sensitisation. Characteristic properties of austenitic stainless steels include good ductility and good weldability. In this thesis, 310 has been used in the corrosion exposures. This is one of the most common austenitic stainless steels for high-temperature service owing to the fact that it has a high chromium content (25 wt.%).

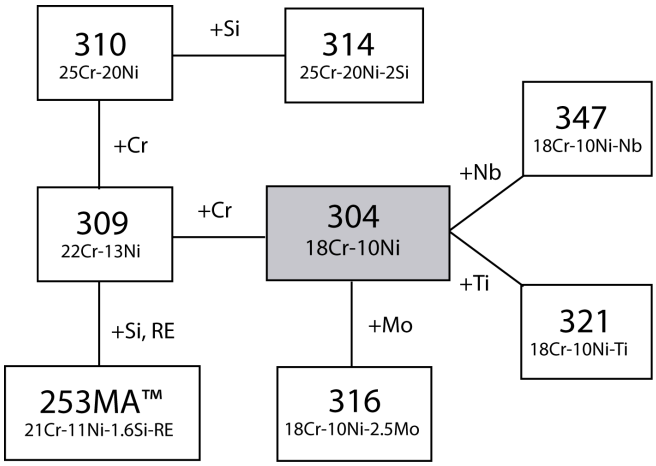

Figure 8 Map showing some of the most common austenitic stainless steels used for high-temperature applications, including their nominal chemical compositions. All the steels have iron as the base. 253MA™ is a trademark of Outokumpu OY.

2.4.2 Ni-base alloys

Ni-base alloys are balanced by nickel, as compared to austenitic stainless steels, which have iron as the base. The nickel content is usually >50 wt.%, even though some alloys have a lower content of nickel but are still considered to belong to the Ni-base family, e.g., Alloy 800HT [65]. The base structure is fully austenitic, and thanks to the high nickel content, good structure stability is maintained even with high concentrations of elements (e.g. molybdenum) that would otherwise impair the structure stability. Ni-base alloys are alloyed with chromium, and in some cases with aluminium to improve their high-temperature corrosion resistance. At high-temperatures, most Ni-base alloys form chromia-scales, although a few, for example Alloy 214, contain sufficient aluminium to form an alumina-scale. Most Ni-base alloys exhibit high mechanical strength. This is accomplished by precipitation hardening through the addition of titanium and aluminium, to form secondary phases such as γ' [Ni_3(Ti,Al)], and also by solution hardening through the addition of molybdenum, cobalt and tungsten [66] [67]. Ni-base alloys are used in various high-temperature applications, including nuclear power plant components, turbine components, and superheaters in power boilers. The high content of nickel and the often advanced manufacturing route make these alloys relatively expensive compared to austenitic stainless steels. Figure 9 shows a map of the most commonly used Ni-base alloys and their nominal compositions, with Alloy 600 considered as the starting alloy. In this thesis, Alloy 690 has been used in corrosion exposures. Alloy 690 has a relatively simple composition with high chromium and nickel contents and low levels of iron and other elements, making it a good candidate for studying corrosion mechanisms.

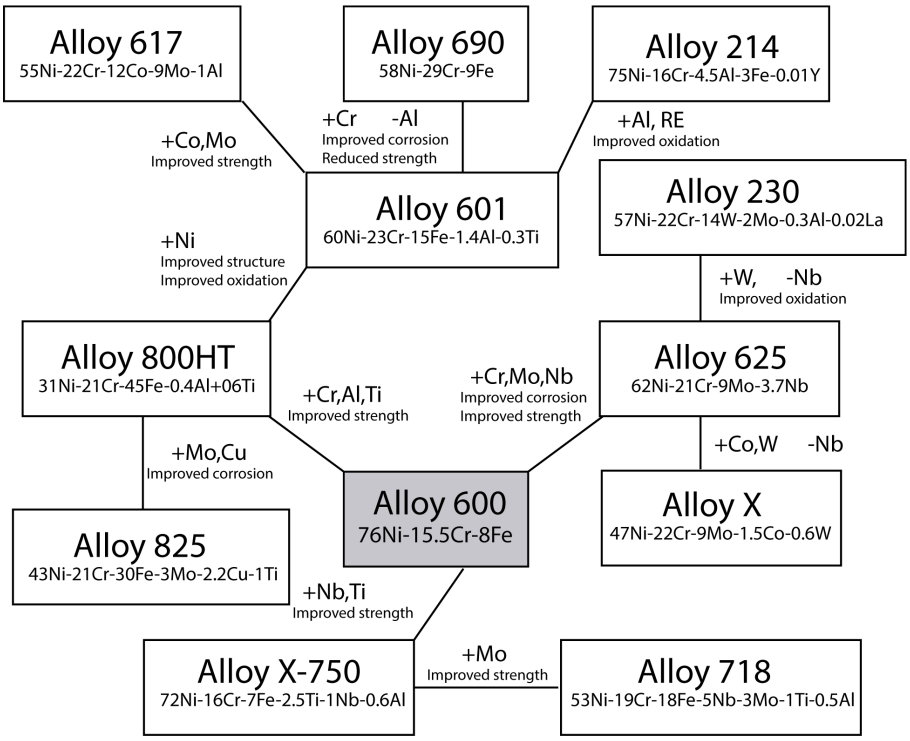

Figure 9 Map of some of the most commonly used Ni-base alloys for high-temperature service. Adopted from [65].

2.4.3 Alumina-forming ferritic alloys

Alumina-forming ferritic alloys are Fe-based alloys that contain aluminium and chromium. These alloys typically have very good oxidation resistance, low thermal expansion, high thermal conductivity, relatively poor weldability, low ductility at room temperature, and poor structure stability. The aluminium is added so that the alloys can form an alumina scale. In the binary Al-Fe system, the aluminium content needs to be approximately 7 wt.% for the alloy to form an external alumina scale [68]. As this would make the alloy very brittle, a third element in the form of chromium is added so that the aluminium content can be reduced to about 3-4 wt.% Al for a Fe-14% Cr [69]. This is called the 'third-element effect'. When the aluminium and/or chromium are on marginal levels to form a continuous alumina scale, it has been observed that Fe-oxide nodules can form [70] [71] [72]. These Fe-oxide nodules do not grow with time due to the establishment of an alumina-scale at the nodule/metal interface [5]. Since a rather high content of chromium is needed for the third-element effect, alumina-forming ferritic alloys are sometimes susceptible to precipitation of secondary phases such as the α'-phase, Cr-carbonitrides, and σ-phase, at intermediate temperatures of 500-800 °C [73] [74]. The formation of α', the so-called 475 °C-embrittlement, involves the separation of the ferritic phase into one chromium-rich phase and one iron-rich phase due to a miscibility gap in the Fe-Cr system. To avoid this, the chromium content should be <11 wt.% in a FeCrAl alloy that contains 4 wt.% Al [75]. However, a composition of 11 wt.% chromium and 4 wt.% aluminium is considered to be marginal for alumina formation [76]. One way to retain the ability to form a protective alumina scale with lower chromium content is to alloy with small additions of silicon [6]. This idea is not new, and using silicon as a third-element in an Fe-Al has been reported before [77]. The silicon is reported to influence the diffusion properties of aluminium and iron and, consequently, increases the ability to form a protective alumina scale.

Another group of elements that is typically used in alumina-forming alloys are REs. In similarity to chromia-forming alloys, increased oxide adherence and a reduced oxidation rate are observed with even small additions of REs (see Section 2.4.4 for a more detailed description of the RE-effect).

In this work, two different alumina-forming alloys were used: Alkrothal® 14, which is typically used in heating applications at temperatures >800 °C and contains 14.4 wt.% chromium and 4.8 wt.% aluminium; and Alloy 197, which contains lower levels of aluminium and chromium but in addition has approximately 1.3 wt.% silicon.

2.4.4 Reactive element effect

REs such as cerium, yttrium, zirconium, tantalum, hafnium, and lanthanum are known to increase the oxidation resistance at high temperature for both chromia- and alumina-forming alloys. Even small additions in the ppm range have been shown to improve the adherence and reduce the growth rates of the formed scales. While the underlying mechanisms are still not fully understood, multiple hypotheses have been put forward, some of which are listed as follows:

- A change in ion diffusivity through the scale, whereby the outward diffusion of cations is reduced and the inward diffusion of oxygen is un-affected, leading to an inward growing oxide that exhibits increased adherence to the substrate and a reduced growth rate [78].
- The RE-particles create a pegging-effect of the oxide to the substrate and increase the adherence of the scale [79].
- The REs act as getters of elements such as sulphur, sodium, and potassium, thereby reducing the levels of these elements in the metal, which otherwise would interact and reduce the adherence of the scale [80].

In a recent study that was performed with a FeCrAl alloy at low pO_2 with traces of H_2O as the single oxidant, it was shown that OH^- was transported through the scale in Y-oxide decorated grain boundaries. The Y-oxide decoration helped to keep the inward transportation path open, and a rather thick alumina was found in the vicinity of the RE-particles [81].

3 MATERIALS AND EXPERIMENTAL

3.1 MATERIALS

Alloys from three groups of materials were used in this work: one austenitic stainless steel, one Ni-base alloy, and two ferritic alumina-forming alloys, see Table 1 for the respective chemical compositions. The austenitic stainless steel 310S is a commonly used high-temperature grade steel, the denotation 'S' indicates that there is no grain size requirement. The Ni-based Alloy 690, hereinafter referred to as A690, has a high chromium content and low iron content. The two ferritic alumina-forming alloys are: Alkrothal® 14 (hereinafter referred to as A14) a commercially available alloy; and Alloy 197 (hereinafter referred to as A197) a newly developed alloy. The main differences between the FeCrAl alloys are the lower chromium and aluminium contents and higher silicon content of A197. Both alloys have low levels of REs added to improve oxidation resistance.

A690 was produced by melting in an Electric Arc Furnace (EAF) followed by continuous casting into a bloom, which was then hot-forged down to a bar with final diameter of 121 mm. The bar was then subjected to a final heat treatment, generating an average grain size of 55 µm. A14 and A197 were produced by EAF-melting, followed by ingot-casting with subsequent hot-rolling into plates. The plates were then cold-rolled into strips with a final thickness of 2 mm. In the final step, bright annealing was applied to ensure a homogeneous microstructure. The manufacturing route for the 310S material is unknown and it was provided as a 1-mm thick strip.

Coupons with nominal size of 12×12×1 mm were cut from all four materials.

Table 1 Chemical compositions of the materials used in this work (in wt.%). Iron is the balance in all cases.

Alloy	*Cr*	*Al*	*Ni*	*C*	*Si*	*Mn*	*Other*
310S	23.8	n/a	19.7	0.044	0.61	1.69	
A690	29.6	n/a	60.1	0.018	0.19	0.29	Ti=0.28
A14	14.8	4.4	n/a	0.03	0.33	0.22	RE
A197	12.4	3.7	n/a	0.02	1.25	0.10	RE

3.1.1 SAMPLE PREPARATION

Prior to exposure, the corrosion coupons were prepared to achieve a homogeneous and smooth surface. Coupons were prepared by grinding the edges with SiC-paper with 1,000 grit. The faces of the coupons were first ground down to 4,000 grit coarseness, and this was followed by polishing with a diamond paste to mirror-bright appearance with a surface roughness of 1 µm. After polishing, cleaning of the coupons was performed in two steps in an ultrasonic bath. In the first step, the coupons were submerged in acetone for 10 minutes, and in the second step they were submerged in ethanol for 10 minutes. The final coupons were then measured for size using a 3-decimal digital caliper and for weight using a 6-decimal scale (Mettler Toledo).

3.2 FURNACE EXPOSURES

High-temperature exposures were performed in electrically heated horizontal tube furnaces that were equipped with reaction tubes of fused SiO_2 with an inner diameter of 44 mm. The set-up of the furnaces is described in Figure 10. The inlet air consisted of ambient air that was filtered by passing the gas through potassium permanganate filters. The flow rate was set between 1,000 ml/min and 8,000 ml/min depending on the exposure, and the gas flow was calibrated using the MesaLabs Defender™ 530+ flow meter. Exposures were performed in both dry air and air that contained 20-40 vol.% H_2O. The air was moistened by bubbling the inlet air in a heated water bath so that it become saturated with water. The saturated air was then passed through a reflux condenser to obtain the desired dew-point of either 60.4 °C for 20 vol.% water content or 76.3 °C for 40 vol.% water content. Calibration of the dew-point was performed with the Michell Instruments Optidew Vision™ chilled mirror humidity sensor. In the horizontal tube furnace, the gas was heated to exposure temperatures in the range of 500-800 °C, depending on the desired exposure. Triplicate samples were placed in Al_2O_3 sample

holders, and parallel to the gas flow direction. For all the exposures, triplicate samples were used. In the reaction tube, the gas first passes a flow restrictor to create a more homogeneous gas flow. Downstream of the samples, the gas is led into a so-called 'Denuder' tube. The denuder tube is coated with $NaCO_3$, which reacts with the evaporated chromium-oxy-hydroxide that is present in the gas stream, according to Reaction 9.

$$CrO_2(OH)_2(g) + Na_2CO_3(s) = Na_2CrO_4(s) + H_2O(g) + CO_2(g) \qquad \text{Reaction 9}$$

The denuder tube was replaced during the exposure so that a time-resolved profile of the evaporation rate was obtained. After the denuder tube had been replaced, it was leached with MilliQ-water and the concentration was assessed by spectrophotometry. The end of the denuder tube was connected to a wash bottle to collect any Na_2CrO_4 that might follow the gas stream and leave the denuder tube. The solution in the wash bottle was subsequently condensed down to about 20-50 ml, and analysed for concentration in the same way as the leached solution from the denuder tube. The gas was heated using heating cords between the condenser and the inlet of the furnace, as well as after the furnace and the end of the denuder tube, to avoid condensation that would otherwise occur below the dew-point of the gas.

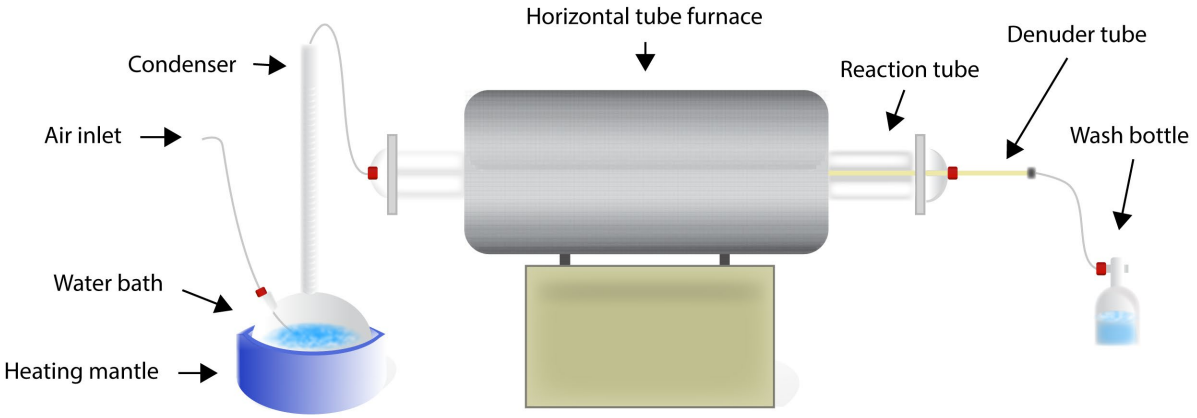

Figure 10 Schematic illustration of the set-up used for the high-temperature exposures.

3.3 Demonstrator exposure

One 400 hours long exposure with A197 was performed in a demonstrator for a small-scale ATR at the company PowerCell Sweden AB. A 0.5 mm thick sample was exposed to the reformate gas (H_2, CO_2, CO, H_2O, CH_4, N_2) on one side, and air with about 40 vol.% H_2O was present on the other side, see the set-up in Figure 11. The temperature was measured at four different positions, at the: wet gas inlet, wet gas outlet, reformate inlet, and reformate outlet, see Figure 12 for the temperature logs for the 400 hour long exposure. During the exposure, three shut-downs occurred. The flow velocity was >5 m/s

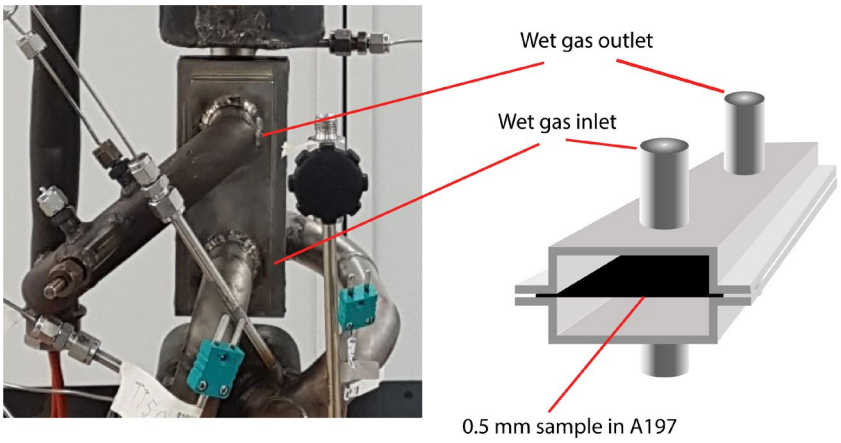

Figure 11 The left panel shows the demonstrator, while the right panel shows how the sample was installed in the demonstrator.

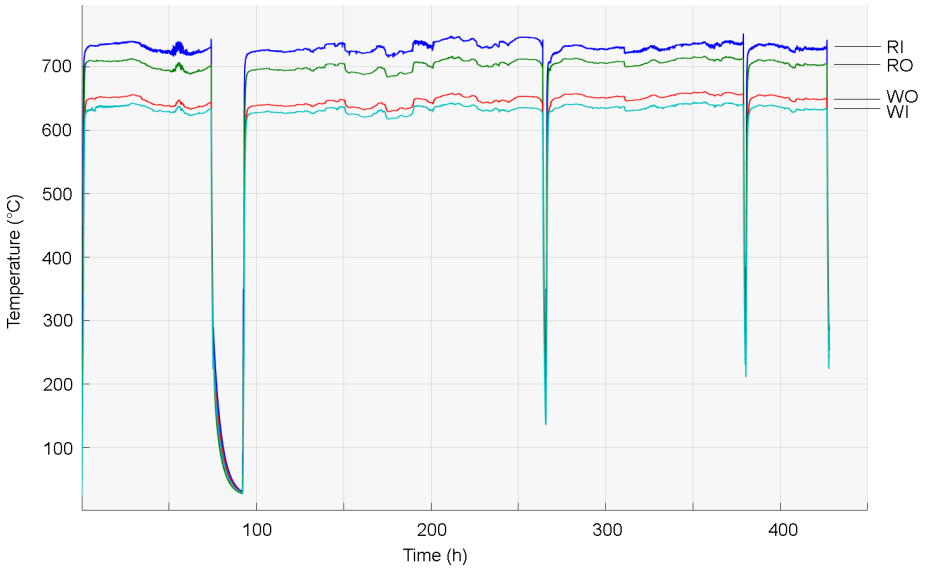

Figure 12 Temperature logs from four different positions during the 400 hour long demonstrator exposure. The positions indicated are: RI, Reformate inlet; RO, Reformate outlet; WO, Wet air outlet; WI, Wet air inlet.

3.4 Sample preparation post-exposure

After exposure, the coupons were weighed using a 6-decimal scale. To avoid contamination from the ambient air, the coupons were stored in a desiccator in the period between the exposure and weight measurement.

The coupons were subjected to different preparation techniques, depending on which type of analysis method that was going to be employed in the subsequent studies. Coupons analysed by X-ray techniques and by plan-view examination using electron microscopy were not prepared, and consequently, they were analysed in the as-exposed condition.

3.4.1 Broad Ion Beam Milling

A Broad Ion Beam (BIB) was used to mill cross-sections of the areas of interest. This technique has the advantage that it removes material without mechanically affecting the sample, thereby avoiding the introduction of artefacts associated with cutting, grinding and polishing. A BIB consists of multiple ion guns that bombard ions onto the metal, thereby removing the material gently. The BIB used in this work was the Leica TIC3X™, which consists of three argon guns. The guns are fixed in a vacuum chamber and directed towards the sample stage where the samples are mounted. A mask is used to select an area of interest, and the ion guns mill away material from the non-masked area. A BIB allows a milling depth of about 1 mm to be achieved in a few hours, making it

a relatively fast and easy tool for the generation of cross-sections. Prior to BIB-milling, the samples were sputtered with a thin gold layer to improve conductivity, and a silicon wafer was glued onto the samples so as to avoid curtain effects [82]. A low-speed cutting saw was used to cut the sample in half before it was placed in the BIB. In the milling process, an applied voltage of 6.5 kV and a current of 2.4 mA were applied.

3.4.2 Focused Ion Beam Milling

Focused Ion Beam (FIB) milling was used to prepare samples for analysis by Scanning Transmission Electron Microscopy (STEM). The principle of this technique is the use of an electron microscope equipped with an ion-gun to perform site-specific, *in-situ* sample preparation. By applying this technique, thin foils from the area of interest can be prepared for further examination, using what is called the 'lift-out' technique. The process steps in the lift-out technique consist of the: deposition of platinum over the area of interest; milling of trenches; performance of a U-cut; and transfer to a copper grid. Further examination of the sample is then performed by Transmission Electron Microscopy (TEM).

In this work, the FEI Versa 3D™ FIB-SEM was used to mill out areas of interest. The FIB-milling was performed by Vijayshankar Asokan.

3.5 Analytic techniques

3.5.1 Spectrophotometry

Spectrophotometry was used to measure the concentrations of solutions that contained CrO_4^{2-} and that were collected using the denuder technique (see Section 3.2). Solutions that contain CrO_4^{2-} have a yellowish colour and absorb light at a wavelength of 370 nm. Spectrophotometry is a technique whereby an incident monochromatic light is passed through a cuvette that contains the solution. The intensity of the transmitted light is then measured by a photometer on the other side of the cuvette. Since the solution absorbs some of the light, it is possible to determine the concentration by measuring the transmitted light. The Beer-Lamberts law, Equation 7, is used to show the relationship between the absorbance and concentration of the solution:

$$A = \epsilon * l * c \qquad \text{Equation 7}$$

where A is the absorbance, ε is the wave-length dependent molar absorptivity, and l is the path length.

To facilitate fast and accurate measurements of a known solution of unknown concentration, a calibration curve can be used. A calibration curve can be prepared using known concentrations of a standard solution and measuring the absorbance. The standard curve used in this work (Figure 13) was created using a Merck chromate standard solution that was diluted with 0.1 M NaOH to obtain various concentrations. The spectrophotometer used was the Fischer Scientific evolution 60s UV/Vis™. The solutions measured were in all cases checked to have a pH >9 to ensure that the ions in the solutions were in the form of CrO_4^{2-}(aq) rather than $HCrO_4^-$(aq) [83].

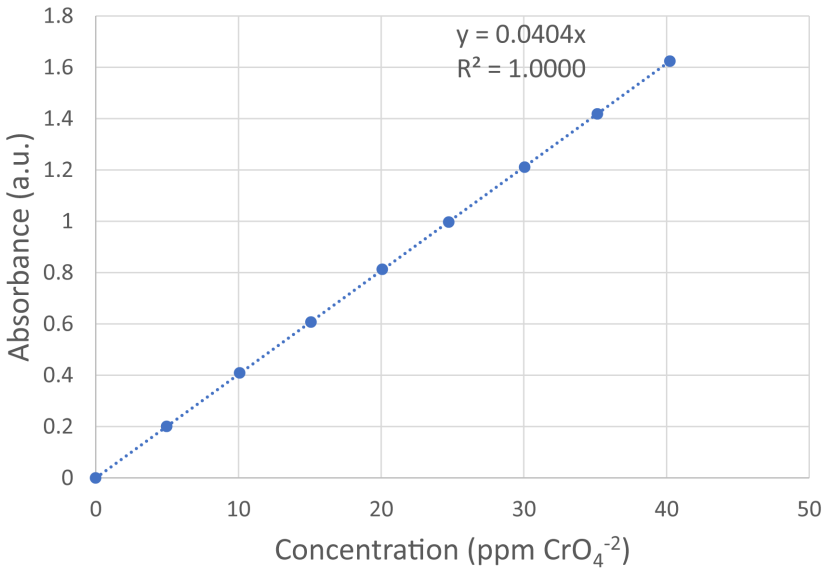

Figure 13 Calibration curve showing the absorbance values for chromate solutions of known concentrations.

3.5.2 X-Ray Diffraction

X-ray diffraction was used to identify the crystal phases of the oxide scales formed after the exposures. Since the oxides formed are crystalline in nature, it is possible to determine the lattice parameter and, thereby, define the crystal phases present in the sample. In X-ray diffraction, a monochromatic X-ray source is used to inflict X-rays of a certain wavelength onto a target sample. In this work, an X-ray source that emitted CuKα-radition with a wavelength (λ) of 1.5418 Å was used. The X-rays are diffracted in the crystal lattice and reflected X-rays fulfilling Bragg's law, see Equation 8, can be detected. See Figure 14 for the principles behind this technique. In Bragg's law, d is the lattice parameter, λ is the wavelength, θ is the incidence/diffracted angle, and n is an integer.

$$n\lambda = 2d_{hkl}sin\theta \qquad \text{Equation 8}$$

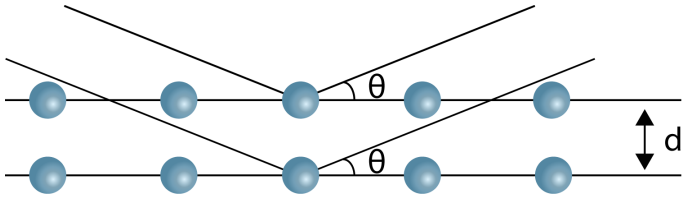

Figure 14 Illustration of the principles of Bragg´s, whereby diffraction in an atom lattice can be used to determine the lattice parameter d.

In Grazing-Incidence X-Ray Diffraction (GIXRD), the source has a fixed incidence angle (0.2°, and 1° in this work) and a moving detector is used to detect the reflected X-rays at different angles. By comparing the measured intensity peaks of the reflected X-rays with powder diffraction files (PDFs), it is possible to determine the crystalline phases present in the examined sample. Since GIXRD can be used with a low incidence angle, the penetration can be limited to shallow depths, making it suitable for analysing oxide scales that are formed on metal surfaces. In this work, the Siemens D5000 GIXRD equipped with a Göbel mirror was used.

3.5.3 Scanning electron microscopy

Scanning electron microscopy (SEM) was used to analyse the oxides formed during the exposures. SEM resembles an optical microscope but instead of light, electrons are used to analyse the sample surface. This makes it a useful technique for examining both the surface topography and chemical composition.

In SEM, electrons are emitted from an electron gun, and then accelerated and focused in a column before interaction with the sample surface. The electrons can be focused so that the SEM has a lateral resolution of

about 1 nm [84]. However, due to the high energy of the electrons, an interaction volume into the sample of about 1 µm is usually obtained. The focused electrons can be scanned in the x-y direction, generating a 2-dimensional image of the surface.

The interaction of electrons with the sample results in various signals, such as secondary electrons (SE), back-scattered electrons (BSE), and characteristic X-rays [84]. SE are electrons that are emitted from the outer scales of atoms when they are subjected to in-elastic scattering of the impacted electrons, see Figure 15a. If these secondary electrons acquire sufficient kinetic energy, they can leave the surface and be detected. Typically, this can only happen for the outer layer of atoms, with the result that a good topographic image can be derived from these electrons.

BSE are electrons that have originated from the electron gun, entered the material, and due to elastic scattering have changed path in the material as a result of interactions with the atoms in the material, see Figure 15b. As these electrons have higher energy levels than SE, they can be distinguished. Denser atoms with higher atomic numbers (Z) generate a higher number of BSE, creating contrast differences in the final image, which provide information about atom density. The interaction volume from BSE is significantly larger than that from secondary electrons, which means that the information obtained comes from a volume deeper within the material.

Characteristic X-rays are generated when an electron excites electrons out of an orbit in one of the material atoms. This induces electrons from outer orbitals to fill the place of the excited electron and emit X-ray photons. As the energy of the emitted X-ray photons is characteristic for a specific orbital movement in a specific element, it is possible to identify the element by analysing the photon energy detected. This mechanism can occur relatively deep within the material, and might not be related to the images generated by secondary and back-scattered electrons. The technique to determine elemental composition using characteristic X-rays is called Energy-dispersive X-ray Spectroscopy (EDS).

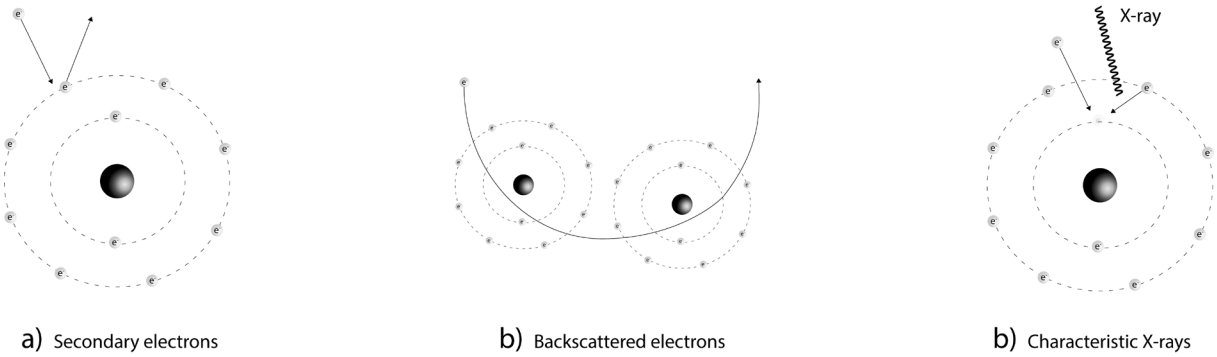

Figure 15 Illustration showing how (a) secondary electrons, (b) back-scattered electrons, and (c) characteristic X-rays are generated in SEM.

In this work, a Quanta 200™ SEM equipped with a Field Emission Gun (FEG) was used. An acceleration voltage of 10-20 kV was used for imaging and one of 20 KV was used for EDS-analysis. For high-magnification imaging, the Zeiss Ultra 55™ FEG-SEM with acceleration voltage of 2 kV was used.

3.5.4 Transmission electron microscopy

TEM was used for detailed investigations of the oxide scale formed. In TEM, electrons are accelerated onto a specimen in a similar way as for SEM, although in TEM the electrons are transmitted through the specimens and apertures are used to interpret the signals on the other side of the specimen. This ensures less interference of the beam compared to when electrons are back-scattered from the specimen, and consequently, the resolution is higher. STEM is a mode in which the electron probe is scanned over the area of interest. In STEM mode, an Annual Dark-Field (ADF) detector is used to create an image of the selected area using serial imaging [85].

The specimens need to be thin for the electron beam to be transmitted through the specimen, typically <100 nm, although in some cases <50 nm [85].

The STEM analysis in this work was performed by Vijayshankar Asokan.

3.5.5 X-RAY PHOTOELECTRON SPECTROSCOPY

X-Ray Photoelectron Spectroscopy (XPS) was used in this work to analyse the chemical gradients in the formed oxide scales. In XPS, X-ray photons are inflicted onto an area of interest. In this work, a beam size of 100 µm was used, representing the lateral resolution. The electrons emitted from the surface are collected using an electrostatic lens. The binding energy can be calculated from the kinetic energy of the electrons, which is converted to chemical information by an energy analyser. The acquired information includes not only the chemical composition, but also the oxidation states of the different atoms. The depth resolution is a few nanometres, making it a suitable analytical tool for surface characterisation [86]. Depth profiling was accomplished by etching the area of interest using Ar-sputtering. The nominal etching rate is 58.5 Å/min in a reference sample of Ta_2O_5.

The XPS analysis in this work was performed by Yu Cao using a PHI5500™ equipped with an AlKα-source.

4 RESULTS AND DISCUSSION

The Results and Discussion section of this work is divided into two parts. In the first part, chromium evaporation and oxide scale evolution of chromia-forming alloys are presented and the results considered. The second part presents and discusses the results obtained from the exposures of the alumina-forming ferritic alloys.

4.1 CHROMIA-FORMING ALLOYS

Evaporation of chromium-oxy-hydroxide from chromia-forming alloys has been studied extensively in the past. It is known that relatively high levels of volatile species are released even at intermediate temperatures, e.g., 600 °C [4].

4.1.1 THE EFFECT OF TEMPERATURE ON CR-EVAPORATION OF A690

To elucidate the ways in which Cr-evaporation is influenced by temperature, A690 was exposed in air with 20 vol.% H_2O with a gas flow rate of 1,000 ml/min in the temperature range of 500-800 °C for 90 hours. By capturing the evaporated species, it was found that even at 500 °C the accumulated level of evaporated species was significant compared to the net mass change. Increasing the temperature resulted in an exponential increase in the levels of evaporated species, see Figure 16. At 700 °C and 800 °C, this also resulted in negative net mass changes after the 90-hour exposures. It should also be noted that the levels of chromium-oxy-hydroxide evaporation in these cases were limited by the relatively low gas flow rates applied during the exposures.

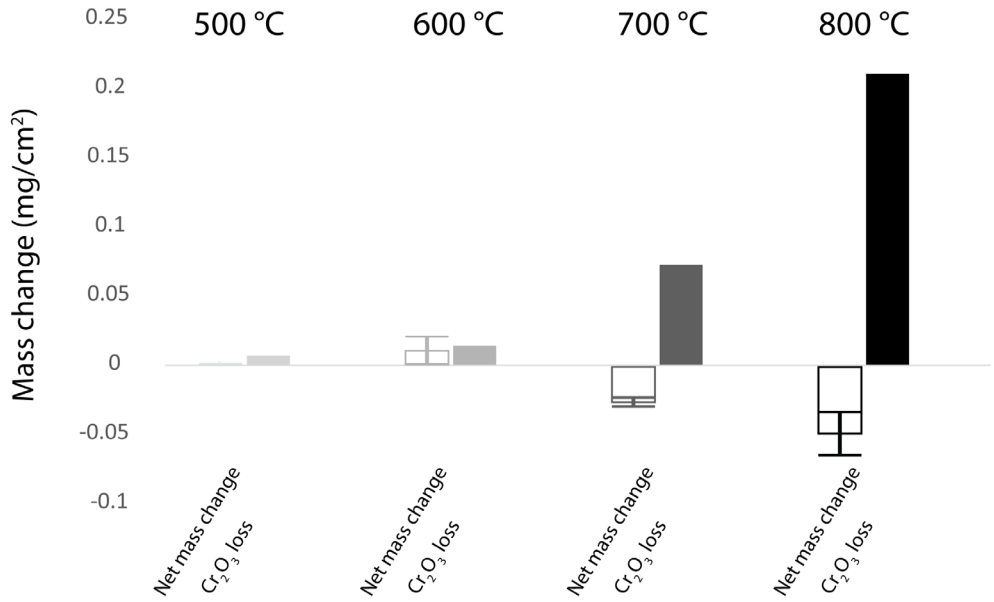

Figure 16 Net mass changes and accumulated losses due to evaporation of chromium-oxy-hydroxide after a 90-hour exposures in air/20 vol.% H_2O at different temperatures. Error bars for triplicate samples are indicated for net mass changes.

An examination of the rates of evaporation of chromium-oxy-hydroxide during the 90-hour exposures (Figure 17) reveal that in all cases the rate of evaporation is high initially and thereafter decreases with time. This is suggested to be due to that the chromium rich oxide formed at the beginning of the exposure is a purer form of chromia and that more Ni, Mn and Fe are ending up in the outer part of the scale, see the XPS-measurements in **Paper I**. It is also likely that an oxide scale with a larger surface area and with more whiskers and blades is formed at the beginning of the exposure, with the surface area being reduced with time, thereby reducing the evaporation rate.

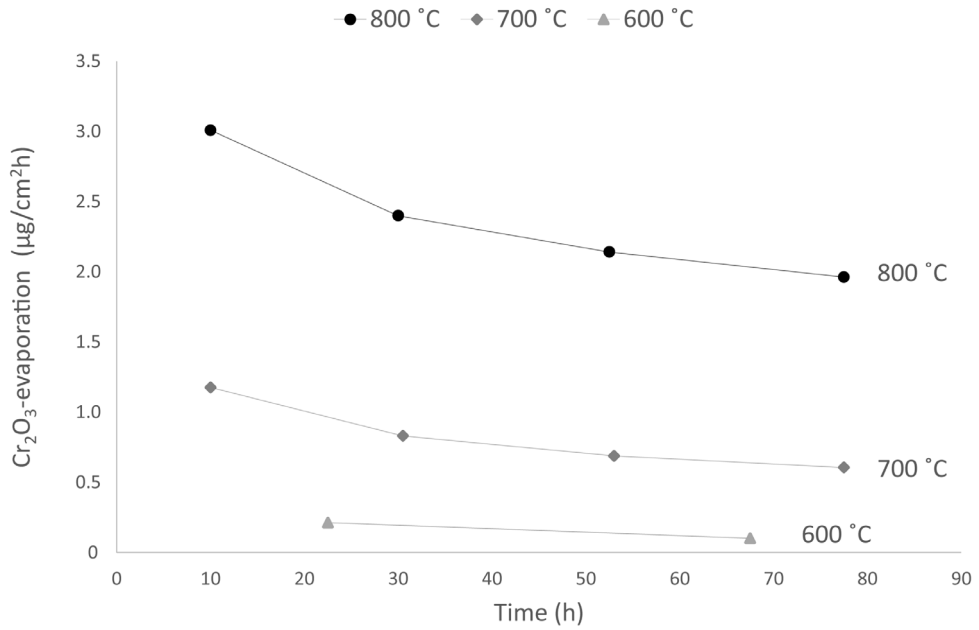

Figure 17 Rates of evaporation of chromium-oxy-hydroxide during the 90-hours of exposures in air/20 vol.% H_2O and with a gas flow rate of 1,000 ml/min at 1 atm and 25 °C. Each denuder replacement is represented by a value, while the lines are for graphical illustration only.

4.1.2 The effect of gas flow velocity on Cr-evaporation of A690

Since the saturation pressure of $CrO_2(OH)_2$ is low, increasing the gas flow rate pushes the reaction for formation of $CrO_2(OH)_2$ from equilibrium, thereby increasing the levels of evaporated species. To evaluate the influence of the gas flow rate, exposures were performed at 800 °C with different gas flow velocities. The rates of evaporation observed at the different gas flow velocities are presented in Figure 18. With increasing gas flow velocity, the evaporation rate increased as expected. Interestingly, the evaporation rate decreased faster at the highest gas flow velocity. After about 180 hours, the evaporation rate for the exposure at 31.6 cm/s was even lower than that for the exposure at 23.7 cm/s.

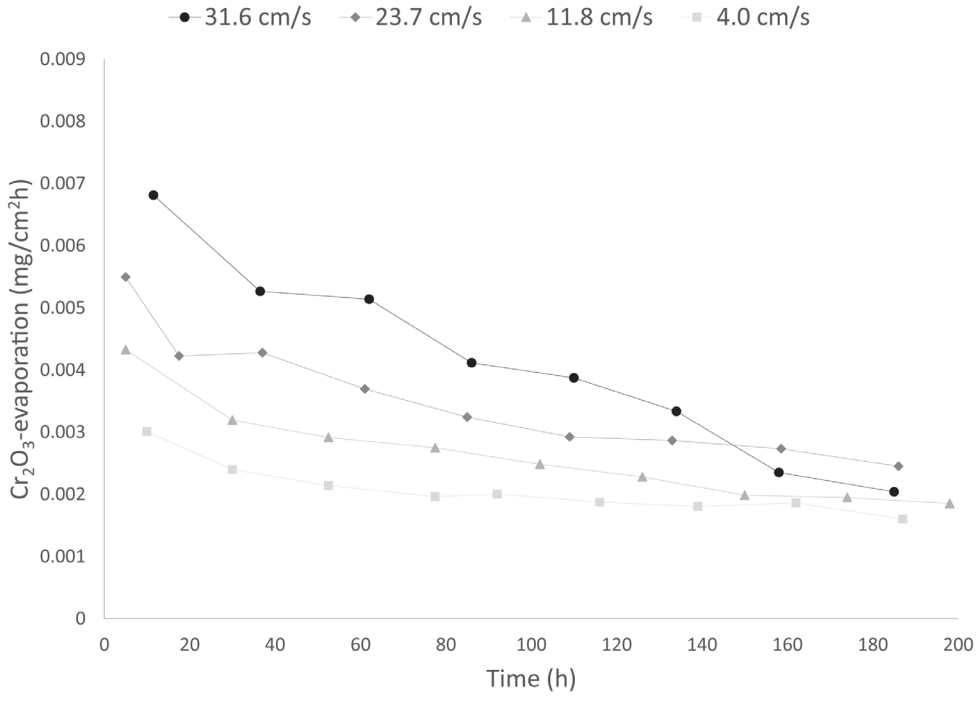

Figure 18 Rates of evaporation of chromium-oxy-hydroxide during 200 hours of exposures in air/20% H_2O at 800 °C with different gas flow velocities. Each denuder replacement is represented by a value, while the lines are for graphical illustration only.

After the exposures for 200 hours with the different gas flow velocities presented in Figure 18 were terminated, the surface oxide scales of the corrosion coupons were examined, see Figure 19. The exposed coupons showed different oxide morphologies. The coupon exposed at the lowest flow velocity, i.e., 4.0 cm/s, exhibited a homogeneous dark oxide scale. At higher gas flow velocities, a brighter oxide scale was observed with more extensive area coverage as the gas flow velocity increased. These different areas are hereinafter referred to as the 'dark area' and 'bright area', respectively. The interface between the bright area and the dark area is represented by the red box in Figure 19, together with the corresponding top-view SEM-SE image. It can be observed that the bright area has oxide islands covering the alloy grains, while the dark area completely lacks this feature. In the area that is more centred in the bright area, i.e., the blue box in Figure 19, the alloy grain boundaries are also covered by the brighter oxide morphology.

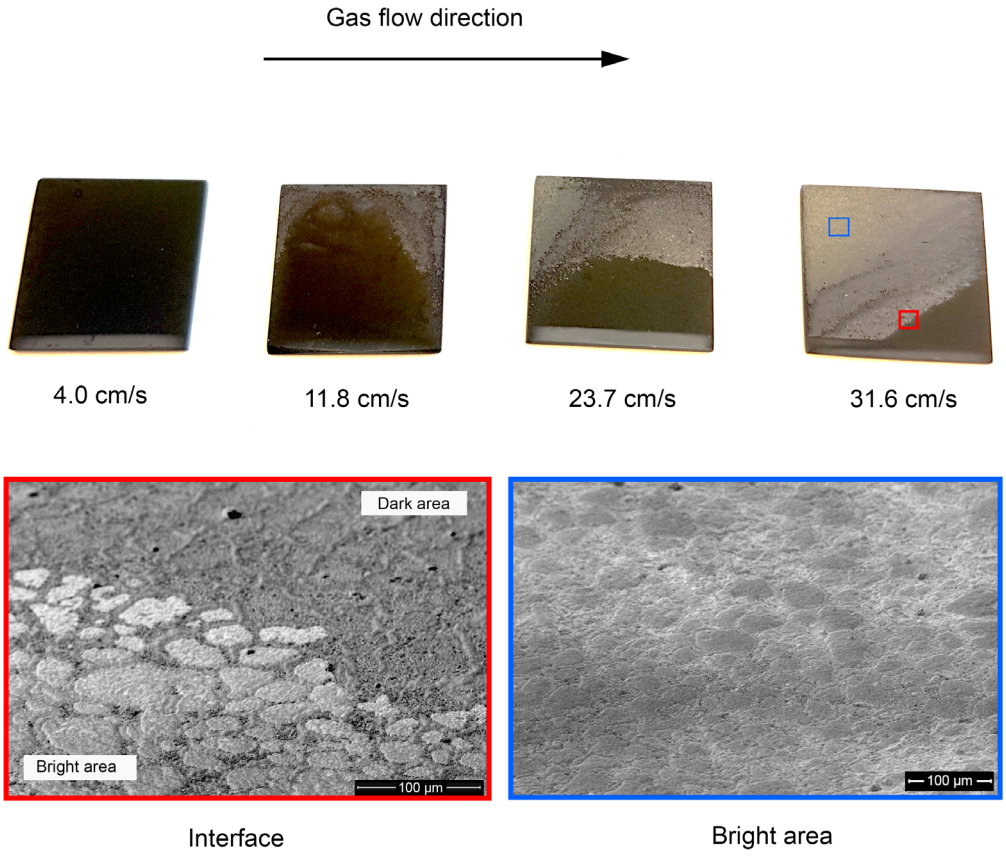

Figure 19 Top, photographic images of samples after exposure for 200 hours in air/20 vol.% H_2O at 800 °C and with different gas flow velocities. The gas flow direction during the exposures is indicated. **Bottom,** SEM-SE top-view images of the red- and blue-boxed areas from samples exposed to a gas flow velocity of 31.6 cm/s.

A cross-sectional SEM-BSE image of a coupon exposed to a flow velocity of 4.0 cm/s is presented in Figure 20. An approximately 0.8 µm thick, continuous, dense, and adherent oxide scale is observed. The oxide contains mainly Cr with low levels of other metallic elements, such as Fe and Ni. This oxide is expected to experience a high degree of Cr-evaporation due to the high concentration of Cr that is in contact with the environment. Some Cr-depletion can also be observed beneath the oxide scale.

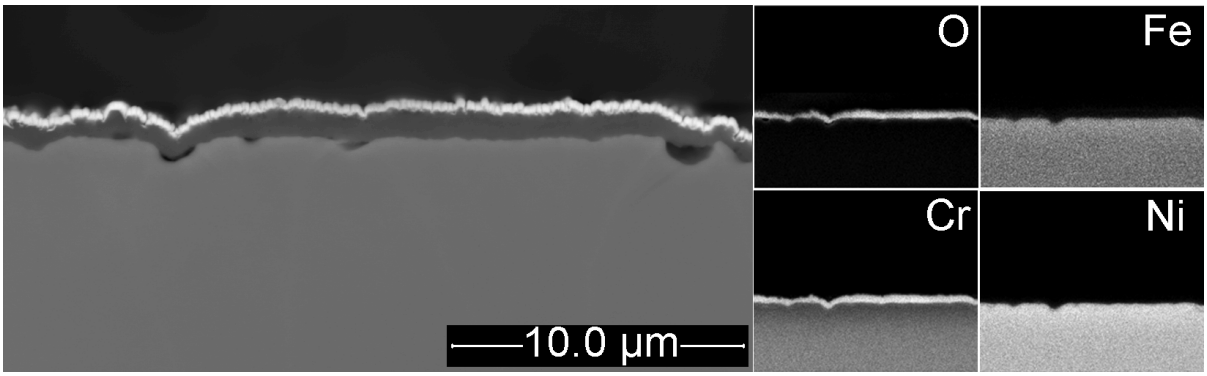

Figure 20 Cross-sectional SEM-BSE image and EDS-mappings showing the oxide scale formed after 200 hours of exposure in air/20 vol.% H_2O and a gas flow velocity of 4.0 cm/s

The dark area that results from exposure at the highest flow velocity, i.e., 31.6 cm/s, also shows a relatively pure chromia scale with low levels of Fe and Ni, see Figure 21. The oxide has a thickness of approximately 0.5 µm, while it is slightly thicker at the alloy grain boundaries. Furthermore, extensive Cr-depletion is evident beneath the scale and in the alloy grain boundaries. This scale is thinner than the scale formed at the lower flow velocity (see Figure 20), and the extent of Cr-depletion is also greater, implying that this area has been subject to more extensive evaporation of chromium-oxy-hydroxide. Furthermore, the low levels of other metallic elements in the scale indicate that Cr-evaporation from this area remains high, depending on the exposure conditions. The Cr content of the alloy was found to be about 12-20 wt.% in the near-oxide region (for more details, see **Paper I**).

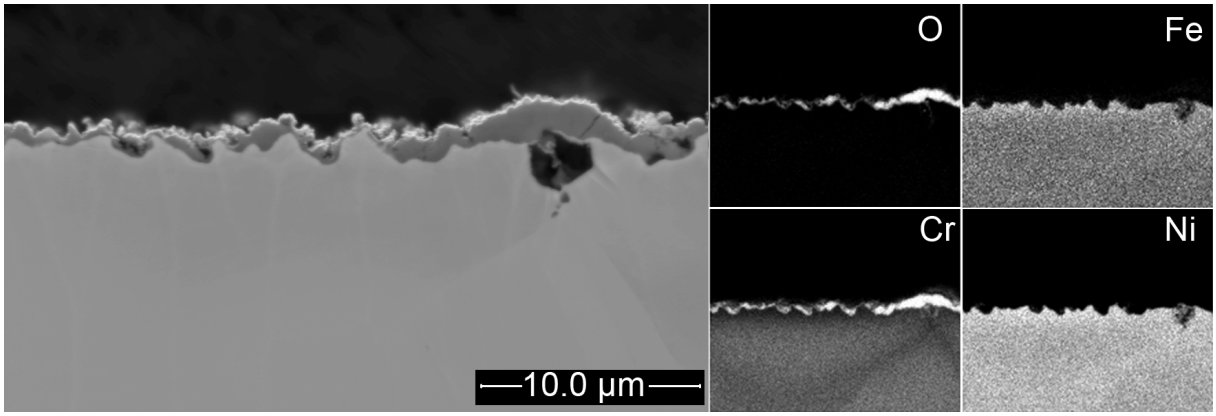

Figure 21 Cross-sectional SEM-BSE image and EDS-mappings showing the oxide scale formed in the dark area after 200 hours of exposure in air/20 vol.% H_2O and a gas flow velocity of 31.6 cm/s.

The scale microstructure in the bright area that results from the exposure at 31.6 cm/s is presented in Figure 22. In this area, the scale consists of three layers, with the top layer showing a close to 50:50 atomic composition ratio of Ni to oxygen, indicating almost pure NiO. The middle layer consists of a mixture of Cr, Ni, and Fe-oxides, which are proposed to be different M_3O_4 phases. The third layer, the one closest to the metal interface, is a high Cr-containing oxide that is suggested to comprise rather pure Cr_2O_3. At the alloy grain boundaries, a slightly different oxide scale is formed, with mainly the outer layer of NiO and inner layer of chromia being observed. Since the amount of Cr is very low in the outer layer of the scale, this oxide is assumed to experience a low level of evaporation of chromium-oxy-hydroxide. The formation of this scale microstructure is probably the reason for the dramatic drop in evaporation rates in the exposures with higher gas flow velocities. The approximately 1 µm thick chromia scale closest to the oxide/metal interface should also be noted. This chromia scale is dense and is suggested to act as a robust diffusion barrier.

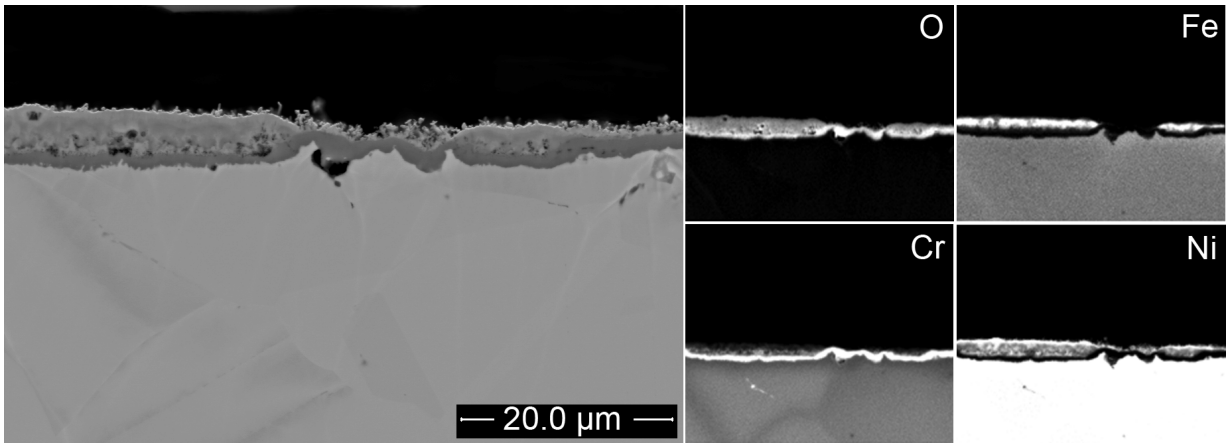

Figure 22 Cross-sectional SEM-BSE image and EDS-mappings showing the oxide scale formed in the bright area after 200 hours of exposure in air/20 vol.% H_2O and a gas flow velocity of 31.6 cm/s.

A dramatic difference is evident in the oxide microstructure between the dark and the bright areas. The higher degree of surface coverage seen at higher flow velocities where the Cr-evaporation is more extensive indicates that this is triggered by Cr-depletion of the metal. When the Cr content of the alloy reaches a critical value, around 12-20 wt.%, break down of the Cr-rich oxide scale occurs and oxidation of Ni and Fe occurs. The breaking down of the Cr-rich oxide scale leads to faster oxidation and enrichment of Ni in the outer part of the scale, which eventually leads to the formation of a rather pure NiO. This 'cap'-layer dramatically reduces the evaporation of chromium-oxy-hydroxide. When the evaporation of Cr species ceases, and Cr is no longer being consumed, the Cr content of the metal near the oxide/metal can recuperate through diffusion and thereby form a secondary chromia-layer. This secondary chromia acts as a strong diffusion barrier and reduces the oxidation rate, see Figure 23 for an illustration of the proposed mechanism. In less-aggressive environments, as in the case with the lowest flow velocity, Cr is continuously supplied to the scale through diffusion, and since the evaporation rates are lower, a critical level of Cr-depletion is not reached. For the 200 hour long exposure, the Cr-rich oxide scale can be sustained, leading to rather constant evaporation rates. It is unclear as to whether and when the Cr levels reach the thresholds to trigger the oxidation of Fe and Ni under the low flow velocity conditions, since Cr is continuously supplied to the oxide/metal interface through diffusion.

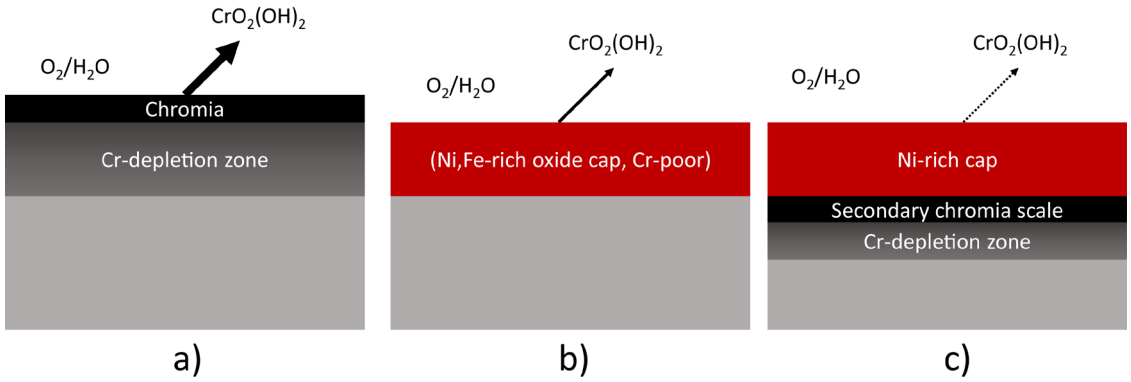

Figure 23 Illustration showing the proposed oxidation and evaporation mechanisms. a) The initial chromia is evaporated, with Cr-depletion of the alloy substrate as a consequence. b) The chromia layer breaks down, leading to the oxidation of Ni and Fe, thereby reducing Cr-evaporation. c) The Ni-rich cap-layer is established, minimising Cr evaporation so that a secondary chromia scale can form.

The microstructure of the final scale formed in the bright area is considered to be protective against both the evaporation of chromium-oxy-hydroxide and excessive oxidation. This is attributed to the high Cr content of 30 wt.% in A690. If a Ni-base alloy with a lower concentration of Cr would have been used instead, a different scale microstructure is anticipated. For example, the Cr-leaner Alloy 600, which has only about 16 wt.% Cr, is not expected be able to establish the secondary chromia scale. This means that under similar exposure conditions it

would remain in Stage b shown in Figure 23, experiencing rapid oxidation. This has been observed in other, similar studies [87].

4.1.3 Exposure of as-exposed A690 samples

The idea of a scale microstructure that comprises an outer layer of NiO and an inner secondary chromia as corrosion protection against oxidation and Cr-evaporation was tested in a proof-of-concept study. For this, coupons were used that were previously exposed to an environment that caused extensive Cr-evaporation and in which the Ni-rich cap layer was formed. These coupons had been exposed for 200 hours in 42 vol.% H_2O with a gas flow velocity of 11.8 cm/s at 800 °C, and it was estimated that about 60-70% of the area was covered by the bright surface oxide. The as-exposed coupons were then exposed at 700 °C in air/20 vol.% H_2O with a gas velocity of 3.6 cm/s for 90 hours. The levels of Cr-evaporation and oxidation were significantly reduced, see Figure 24, together with the results from as-polished coupons exposed for 90 hours under the same conditions at 700 °C and 600 °C.

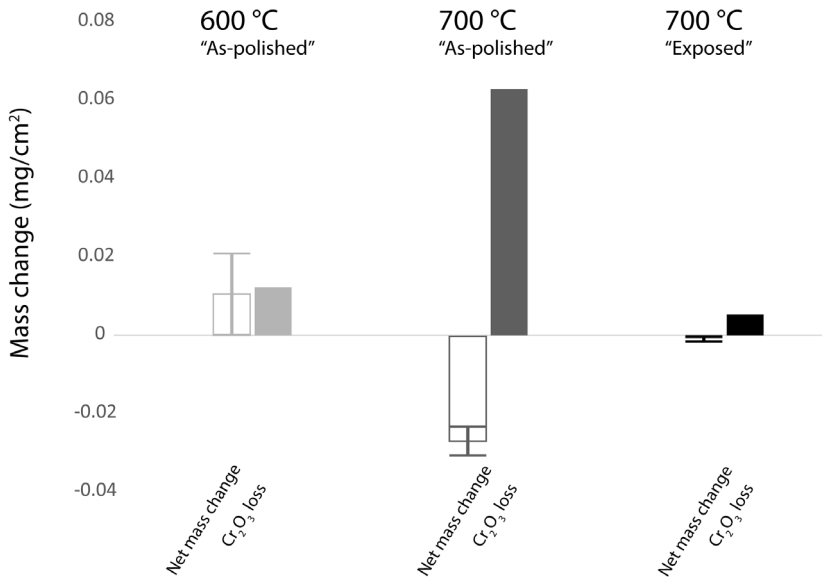

Figure 24 Net mass changes and Cr_2O_3 losses after 90 hours of exposure of 'as-exposed' samples in air/20 vol.% H_2O at 700 °C and a gas flow velocity of 3.6 cm/s, as compared to the results obtained from 'as-polished' coupons. The scatter for the triplicate samples are indicated.

4.1.4 Exposure of 310S in humidified air

The stainless steel type 310S was exposed to an environment that contained air with 40 vol.% H_2O and a gas velocity of 11.8 cm/s for 200 hours, and compared to A690 exposed to the same conditions. The results show that the initial evaporation rate for 310S was about 50% of the rate for A690, see Figure 25. However, after 200 hours of exposure, the evaporation rates were similar. The net mass change after 200 hours of exposure was +0.089 ± 0.023 mg/cm^2, indicating a rather high oxidation rate.

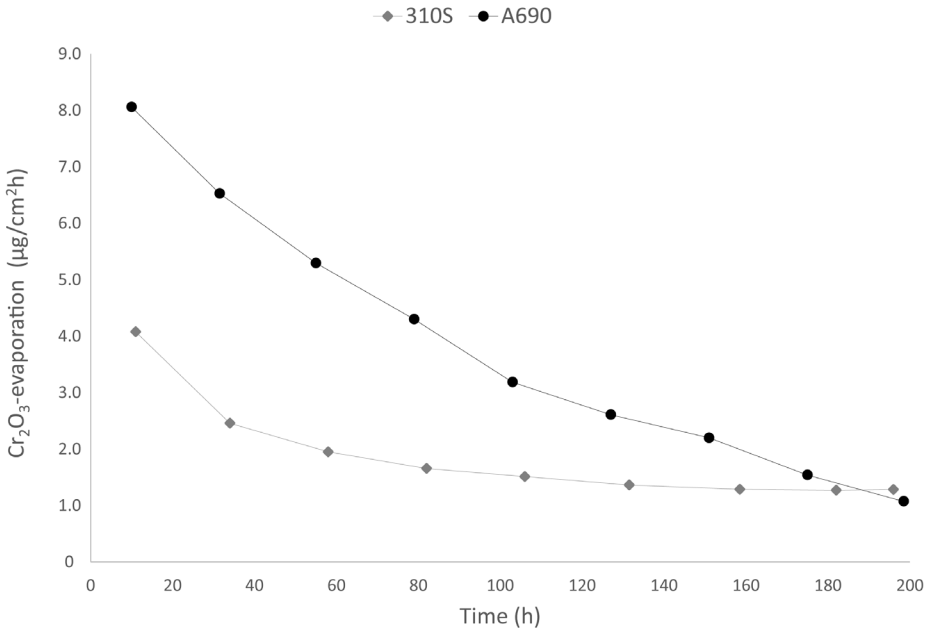

Figure 25 Rates of evaporation of chromium-oxy-hydroxide in 200 hours of exposures in air/40 vol.% H_2O at 800 °C and a gas flow velocity of 11.8 cm/s for the different alloys 310S and A690. Each denuder replacement is represented by a value, while the lines are for graphical illustration only.

An explanation to the much lower evaporation rate in the beginning of the exposure can be observed in Figure 26, where the cross-section of 310S is shown after 20 hours of exposure. The high Mn content in the outer part of the oxide scale indicates a reduced Cr activity closest to the oxide/gas interface. Even though the initial low evaporation rate of 310S indicates better protection against Cr-evaporation, as compared to A690, it is evident that 310S is subject to high oxidation rates in this environment and is less protective than A690. After 200 hours of exposure, islands of Fe-oxide (as observed previously [88]) became apparent on 310S, indicating the start of break-away oxidation (Figure 27). Compared to A690, where a NiO is formed and a new secondary chromia scale is established at the interface between the scale/metal, the break-away oxidation for 310 leads to rapid oxidation of Fe without the ability to form a secondary chromia layer.

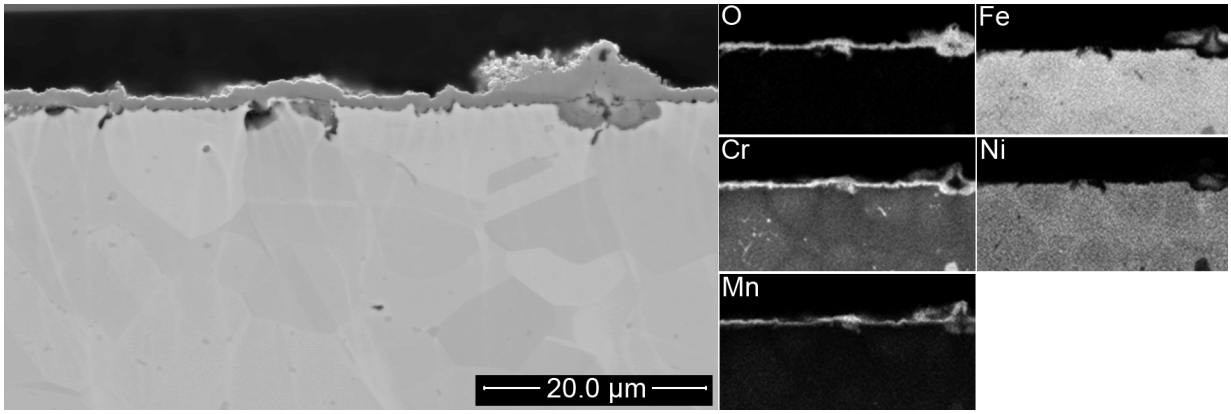

Figure 26 Cross-sectional SEM-BSE image and EDS-mappings showing the oxide scale formed on 310S after exposure for 20 hours in air/40% H_2O and a gas flow velocity of 11.8 cm/s. The scale has an outer layer rich that is rich in Mn and Cr, probably spinel oxide, and an inner layer that contains a low amount of Mn, probably Cr-rich corundum-type oxide.

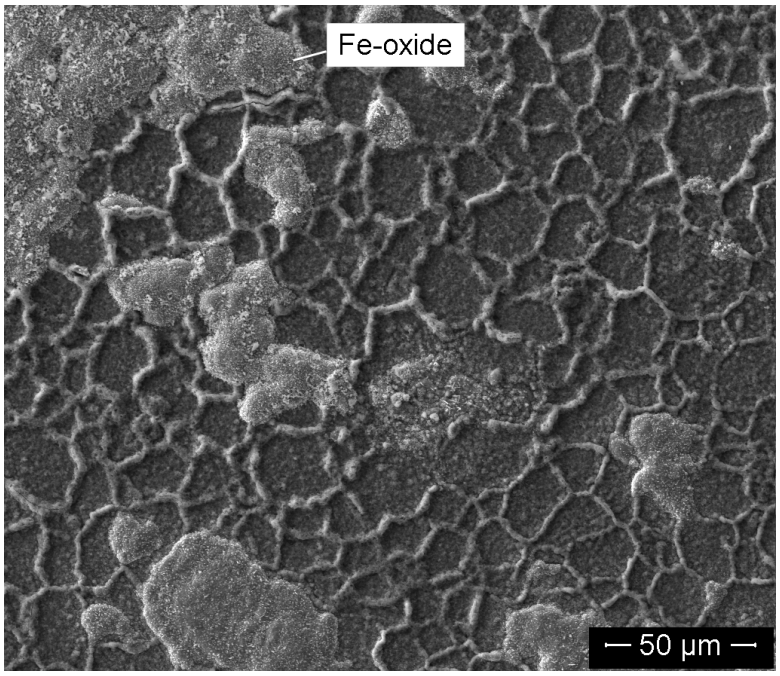

Figure 27 Plan-view SEM-SE image showing 310S exposed in air/40 vol.% H_2O at 800 °C for 200 hours. Areas of Fe-oxide have started to form, indicating the start of break-away oxidation.

4.2 Alumina-forming alloys

Alumina scales have superior protective properties compared to chromia scales. Formation of the highly protective α-alumina scale typically requires temperatures >800 °C, such that the transient alumina transforms into α-alumina. At temperatures ≤600 °C, it is unlikely that the transient alumina will transform into α-alumina. In the present study, the protective properties of two FeCrAl alloys have been studied in the temperature range 600-800 °C in oxidising environment with and without H_2O. One of the alloys, A14, contains higher levels of Cr and Al and, due to embrittlement issues, it is not commonly used at these temperatures. The other alloy, A197, is alloyed with lower levels of Cr and Al but contains approximately 1.3 wt.-% Si, which makes it less susceptible to embrittlement.

4.2.1 Exposures at 800 °C

Initially, the studies were performed at 800 °C, at which temperature it is known that α-alumina can form. The net mass changes after exposure in both dry air and wet air (40 vol.% H_2O) are presented in Figure 28. Both alloys show low, sub-parabolic mass gains, indicating the formation of thin, protective oxide scales. A197 also shows a slightly higher mass gain than A14. At the same time, higher mass gains are observed in wet air than in dry air. This has previously been observed [89] and has been attributed to the stabilization of γ-alumina by water, which has a higher oxidation rate than α-alumina.

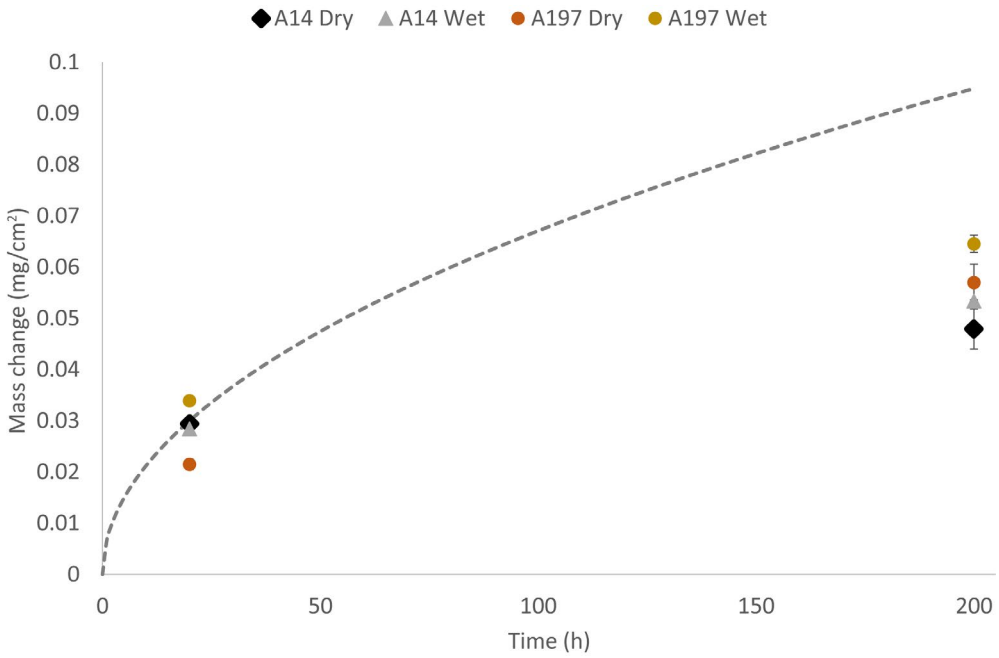

Figure 28 Net mass changes observed for A197 and A14 exposed to dry and wet air for 20 hours and 200 hours at 800 °C. The dashed line is a parabolic help line for the purpose of comparison.

Measurements of Cr-evaporation using the denuder technique showed that both FeCrAl alloys exhibited very low degrees of Cr-evaporation, i.e., 2-3 orders of magnitude lower than that for the chromia-forming alloy 310S (Figure 29). In fact, measured levels of CrO_4^{2-} were close to the detection limit for the experimental set-up used. The very low evaporation rates for the alumina-forming alloys are in agreement with those reported in previous studies [62], and show that even though FeCrAl alloys contain 10-15 wt.% Cr, a negligible amount of Cr is evaporated.

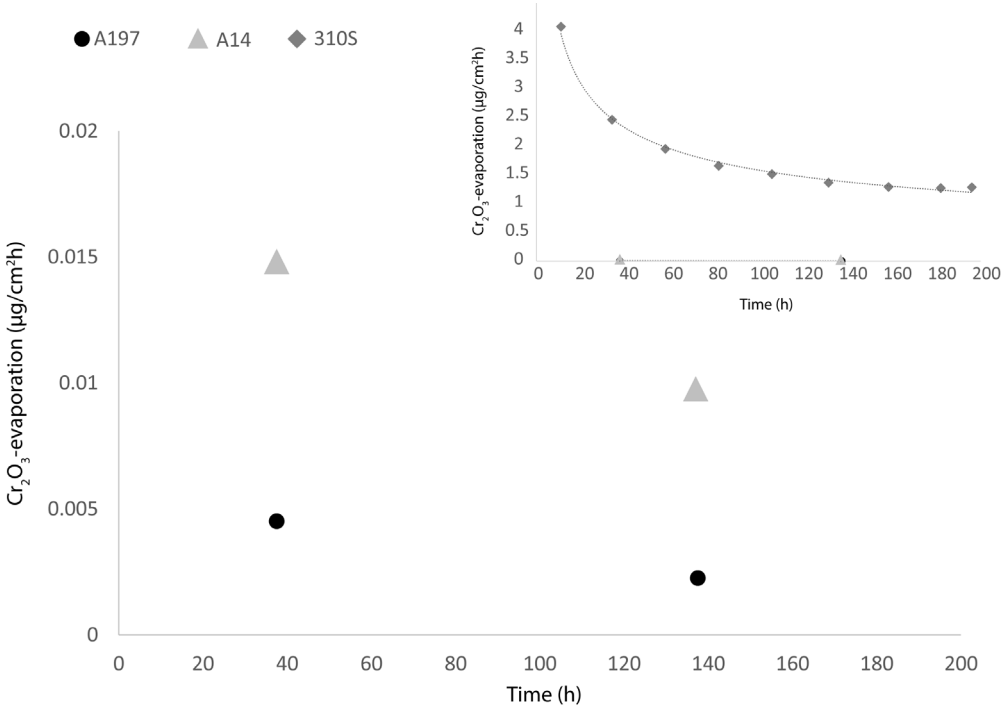

Figure 29 Cr-evaporation rates for A14 and A197 in 200 hours of exposure in air/40 vol.% H_2O and a gas flow velocity of 11.8 cm/s at 800 °C. Inset: Cr-evaporation rates for the chromia-forming alloy 310S under the same exposure conditions (shown for comparison purposes).

As indicated by the gravimetric results, both alloys form thin oxide scales, see Figure 30 for A197 and Figure 31 for A14. In all cases, scales are observed that consists of two layers: a dense inner layer, and a somewhat porous outer layer. The interface between the inner layer and the outer layer is represented in the images by dashed lines. The inner layer is expected to be inward-growing α-alumina, while the outer layer is suggested to be outward-growing transient alumina, in accordance with the findings of previous studies [38]. The inner scale is thicker for A14 than for A197, indicating faster transformation of transient alumina into α-alumina. The outer outward-growing scale is significantly thicker for A197 than for A14.

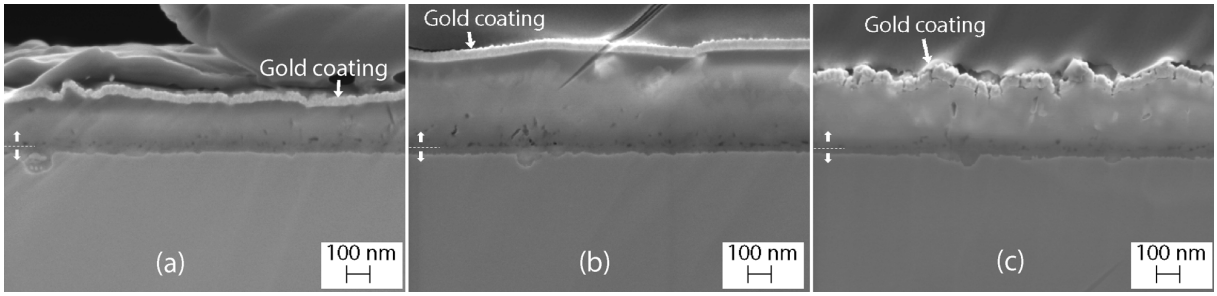

Figure 30 Cross-sectional SEM-SE images of A197 exposed to: (a) wet air for 20 hours; (b) wet air for 200 hours; and (c) dry air for 200 hours. The dashed lines indicate in each case the interface between the inner dense layer and the outer porous layer of the oxide scale.

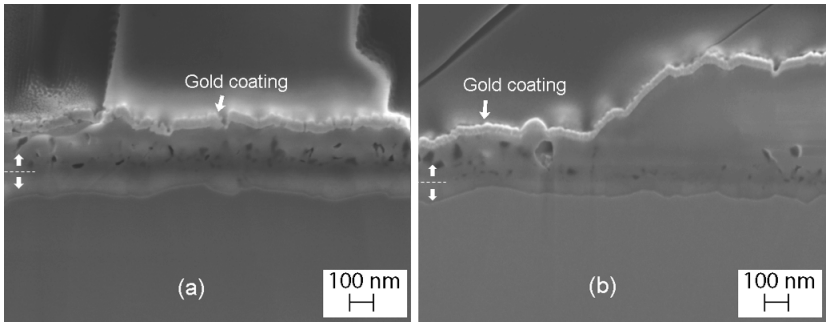

Figure 31 Cross-sectional SEM-SE images of A14 exposed to: (a) wet air for 200 hours; and (b) dry air for 200 hours. In (b), the general oxide is seen to the left side in the image while the right side represent an oxide nodule/ridge at an alloy grain boundary. The dashed lines indicate the interface between the inner dense layer and the outer porous layer of the oxide scale.

The main differences between A197 and A14 lie in the outer layer of the scale. Further examination of the oxide scale formed on A197 in wet conditions after 20 hours was performed by STEM (Figure 32). A remarkably high level of Si is noted in the oxide scale. In the outer part of the scale, the cationic concentration of Si is >60 at.%, while the Al concentration is about 20-30 at.%. Towards the interior of the scale, the Si concentration decreases, while the concentration of Al increases. At a depth of about 160 nm, the remnants of the initially formed transient oxide are observed, with an increased concentration of Cr. Furthermore, the increase in Fe concentration and decrease in Si concentration at about 50 nm are associated with a needle-shaped feature in the oxide scale.

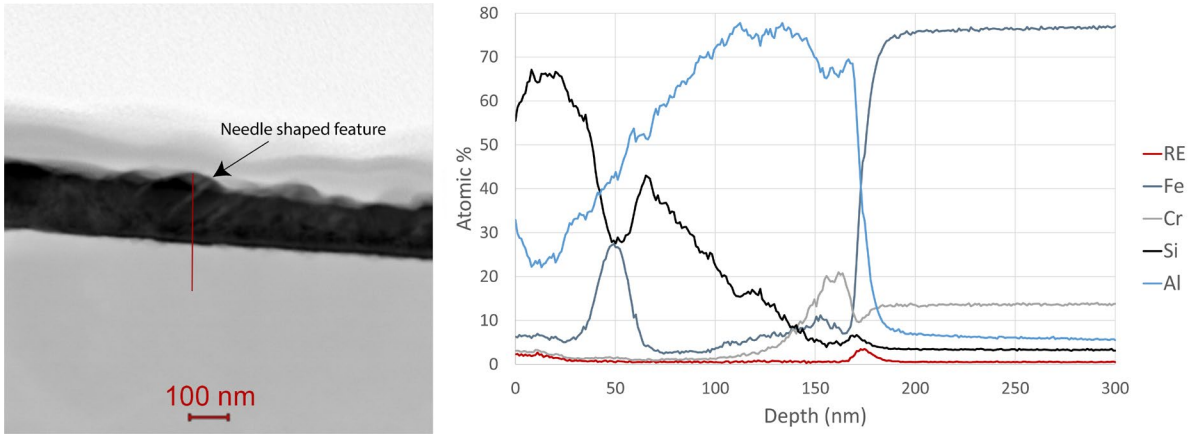

Figure 32 STEM image and line scan of A197 exposed to wet air for 20 hours at 800 °C. The line scan shows the cation concentrations across the oxide, indicating a high level of Al, together with Si.

To verify that the high level of Si observed in the scale by STEM is representative of the entire scale, approximately 0.15 mm^2 areas were subjected to plan-view SEM-EDS analysis. By lowering the acceleration voltage, and thereby decreasing the interaction depth, it was possible to identify a strong signal for Si at the lowest acceleration voltage of 5 kV, see Figure 33. This indicates the presence of a high level of Si in the scale. Interestingly, this was only observed from the exposure in wet air for 200 hours, and not from the exposure in dry air for 200 hours. Furthermore, no peak in Si was observed from the lower Si-containing A14 exposed in wet air.

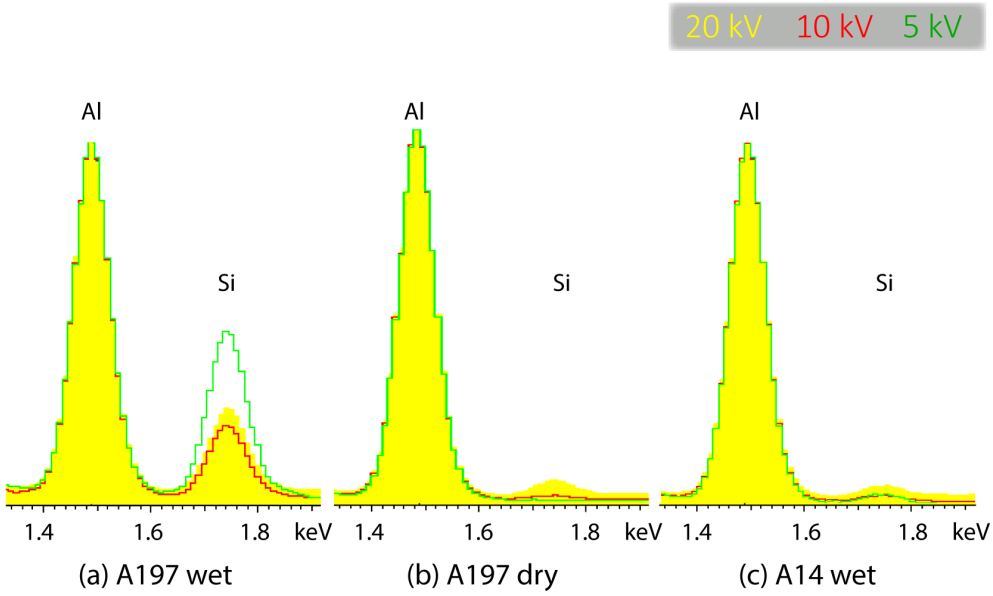

Figure 33 SEM-EDS examination from top view of: (a) A197 exposed in wet air for 200 hours; (b) A197 exposed in dry air for 200 hours; and (c) A14 exposed in wet air for 200 hours. The two peaks show the intensities for Al and Si normalised to Al for three different acceleration voltages: 5, 10 and 20 kV.

GIXRD measurements were performed on the two alloys (A197 and A14) derived from both the wet air and dry air exposures, to determine the crystalline structures of the oxides formed, see Figure 34. The diffractograms for A14 exposed in both wet and dry air, as well as for A197 exposed in dry air are all similar, indicating that the scale consists of α-alumina and γ-alumina. The diffractogram for A197 in wet air is significantly different and shows that in addition to peaks for α-alumina and γ-alumina, there are additional peaks in the 2θ interval of 15-42°. These peaks show good correspondence to the phase mullite $Al_2(Al_{2+2x}Si_{2-2x})O_{10-x}$ and α-tridymite (a high temperature SiO_2 polymorph).

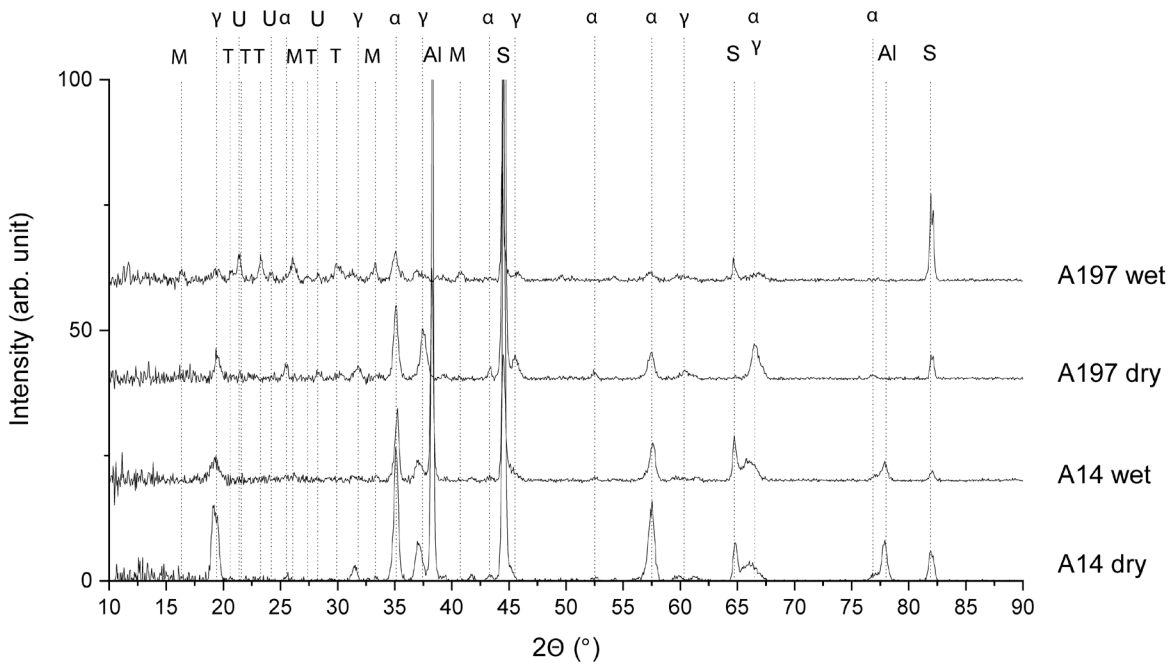

Figure 34 GIXRD-diffractograms for A14 and A197 exposed in dry and wet air for 200 hours at 800 °C. The indicated peaks are: M, mullite; T, tridymite; Al, aluminium; S, substrate; γ, γ-alumina; U, unidentified peak; and α, α-alumina.

4.2.2 Exposures at 600 °C

At 600 °C, both alloys form protective oxide scales, see Figure 35 for the mass gains from exposures in dry air and wet air (40 vol.% H_2O). These mass gains are significantly lower than those seen at 800 °C. As for the exposures conducted at 800°C, the mass gains are higher for A197 than for A14, also at 600 °C. A14 shows a strongly sub-parabolic behaviour, while A197 shows an initial high mass gain. Closer examination of the mass gains for A197 reveals that the mass gain after 200 hours is almost the same as that after 20 hours. This indicates that oxidation is more rapid at the beginning of the exposure but quickly slows down thereafter. Slightly higher mass gains are observed for A197 in wet exposures, as compared to dry exposures.

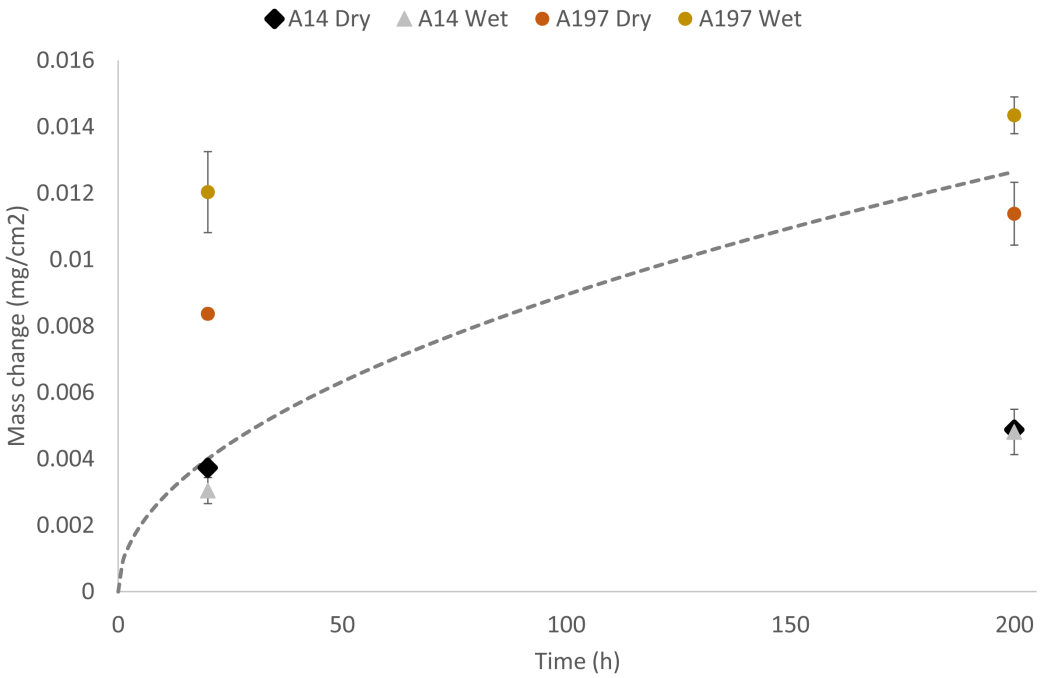

Figure 35 Net mass changes for A197 and A14 exposed in dry air and wet air for 20 hours and 200 hours at 600 °C. The dashed line is a parabolic help line for the purpose of comparison.

The reason for the high mass gain for A197 after 20 hours of exposure is evident by observing top view SEM-BSE images, see Figure 36. For A197, Fe-oxide nodules have formed around the RE-particles. These nodules are proposed to have formed within the first 20 hours of the exposure, contributing significantly to the mass gain. Furthermore, it is suggested that these nodules cease to grow when a protective alumina scale forms at the metal/nodule interface, as indicated in cross-sectional view of the scale, see Figure 37. In this figure, it is also seen that the base oxide has a thickness of about 30 nm, which is considerably less than the 77 nm thick oxide obtained by calculating the expected oxide thickness based on mass gain. This is another indication that the initial relatively high oxidation rate is due to the formation of Fe-oxide nodules. For A14, these nodules are not observed around the RE-particle (see **Paper II**) which is suggested to be due to the higher Al and Cr content for A14 that provides a faster formation of the initial transient oxide in these regions.

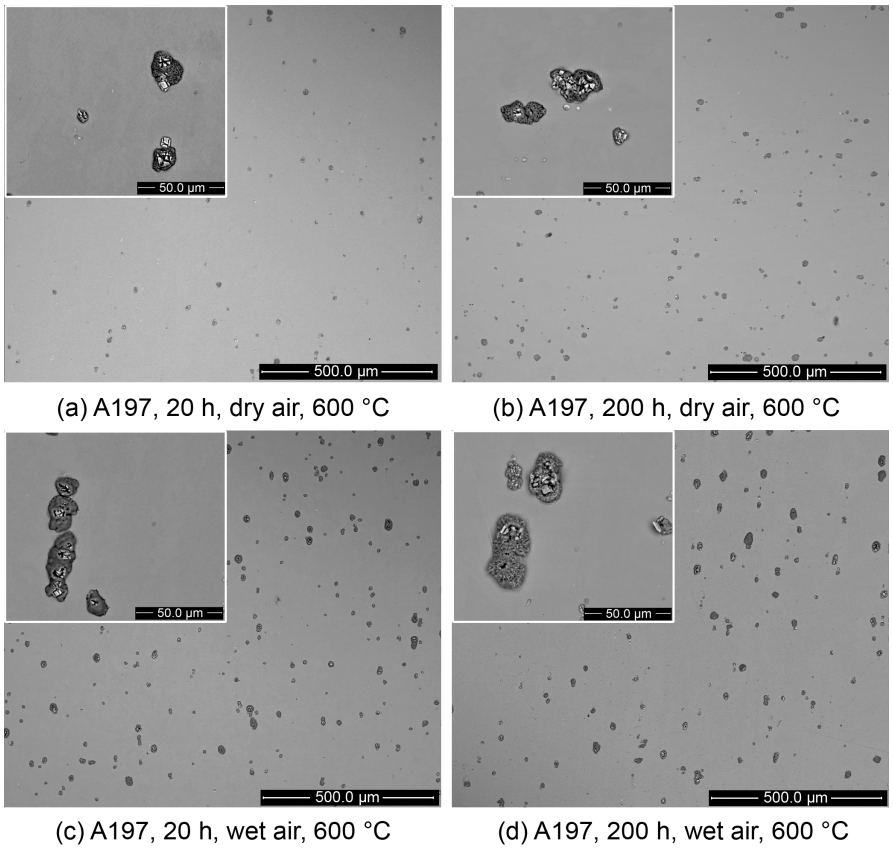

Figure 36 Top view SEM-BSE images of A197 exposed to: (a) dry air for 20 hours; (b) dry air for 200 hours; (c) wet air for 20 hours; and (d) wet air for 200 hours.

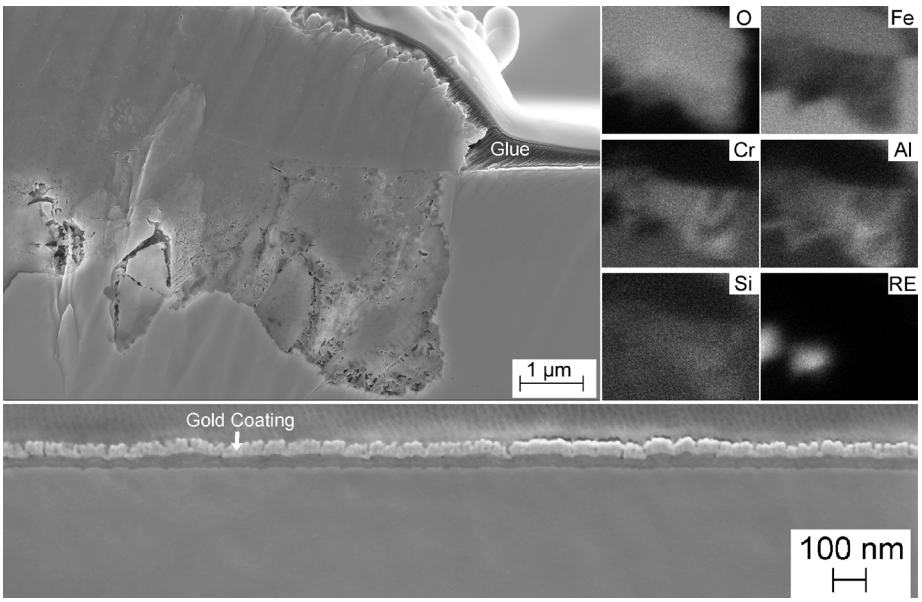

Figure 37 Cross-sectional images showing A197 after exposure in wet air for 200 hours at 600 °C. Top image shows the area at a Fe-oxide nodule. The lower image shows the base oxide.

4.2.3 DEMONSTRATOR EXPOSURE

In the demonstrator exposure, A197 was exposed for 400 hours, whereby one side was subjected to wet air and the other side was exposed to the reformate gas. Since the thickness of the sample is only 0.5 mm, it can be expected that hydrogen on the reformate side can diffuse to the air side, thereby influencing oxidation, by the

so-called ‘dual-atmosphere’ effect [90]. The temperature was in the range of 630-660 °C at the wet gas outlet. Figure 38 shows SEM images of the oxide scale formed on the sample at the wet gas outlet after exposure in the demonstrator. There is a striking similarity between the oxide scale formed in the demonstrator and the oxide scales formed after laboratory exposure, see 4.2.2. In both cases, Fe-oxide nodules are formed and the base oxide thicknesses are similar. This indicates that the material behaves similarly in laboratory studies and field studies, even though the exposure times, flow velocities, and temperatures are somewhat different. It can be observed that the volume expansion of the oxide nodule (see Figure 38b) has caused the metal in the vicinity of the nodule to deform. The stress levels in this region are probably increased during heating/cooling. However, even though the sample has been subjected to three shut-downs, no cracks are observed around the oxide nodules. Furthermore, the similarities between the laboratory exposures and the demonstrator exposures indicate that there is no dual-atmosphere effect in this case.

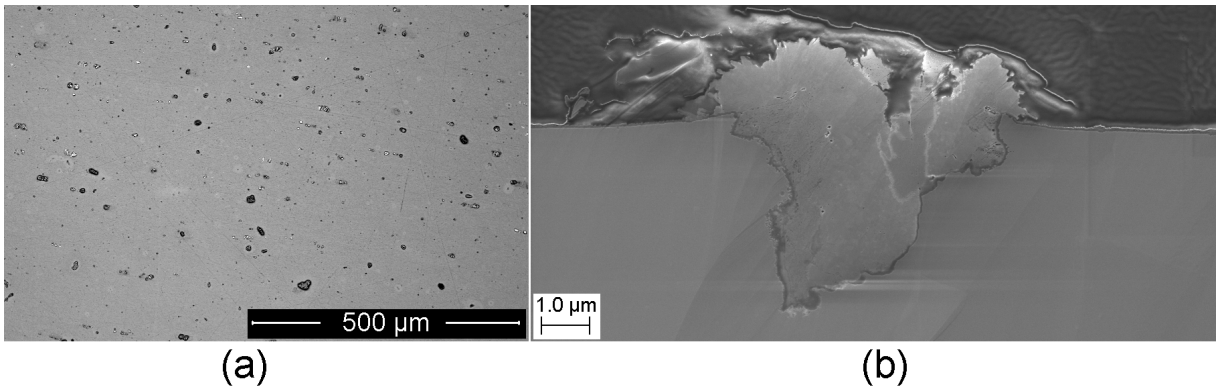

Figure 38 SEM images showing the oxide scale formed on the wet air side after 400 hours of exposure in the demonstrator. (a) SEM-BSE plan-view image. (b) SEM-SE cross-sectional image showing an area containing an oxide nodule.

5 SUMMARY

The main findings from the present work are summarised below, and the most important conclusions are listed.

5.1 CHROMIA-FORMING ALLOYS

Exposing chromia-forming alloys in air with 20-40 vol.% H_2O results in extensive evaporation of chromium-oxy-hydroxide in the temperature range of 500-800 °C. Oxide microstructure evolution varies significantly depending on alloy composition.

Ni-base A690

- When the evaporation rate is moderate, due to a low temperature and/or low gas flow velocity, the oxide scale consists of a corundum-type Cr-rich oxide that experiences high levels of evaporation. A slight decrease in the evaporation rate is observed, which is attributed to the accumulation of other cationic elements in the outer part of the scale, as well as to smoothening of the topography, which reduces the surface area.
- When the evaporation rate is sufficiently high, Cr-depletion leads to break-down of the chromia scale, such that oxidation of Ni and Fe occurs, which reduces the evaporation rate significantly. Recovery of Cr in the alloy leads to the formation of a secondary chromia scale at the scale/metal interface. The microstructure of the final scale is protective against evaporation due to the very low concentration of Cr content in the outer oxide layer, and against further oxidation owing to the formation of the secondary chromia-scale.

Austenitic stainless steel 310S

- The initial evaporation rate of 310S is lower than that of A690 due to the high concentration of Mn in the alloy, which reduces the activity of Cr in the outer part of the scale.
- After break-down of the scale due to evaporation, significant oxidation of Fe occurs, indicating the start of break-away oxidation.

5.2 ALUMINA-FORMING ALLOYS

Two different alumina-forming alloys were exposed in dry air and air/40 vol.% H_2O at 600 °C and 800 °C. One of the alloys had lower contents of Cr and Al but contained about 1.3 wt.% Si.

Exposure at 800 °C

- Both alloys are able to form protective scales with very limited evaporation rates of chromium-oxy-hydroxide. Furthermore, the alloy that contains 1.3 wt.% Si formed an oxide scale that has a high level of Si, >60 cationic-%, locally in the scale. This is only observed when exposures are performed in wet air (and not when exposed in dry air). The GIXRD measurements indicate that the scale contains mullite $Al_2(Al_{2+2x}Si_{2-2x})O_{10-x}$ and α-tridymite (SiO_2).

Exposure at 600 °C

- At 600 °C, both alloys are able to form protective oxide scales, with minimal evaporation of chromium-oxy-hydroxide.
- The formation of Fe-oxide nodules is observed in the vicinity of RE-particles in both the laboratory and demonstrator exposures. These oxide nodules are suggested to form in the early stage of oxidation, with no apparent growth after 20 hours. The reason for the Fe-oxide nodules to stop growing is proposed to be that a protective alumina has been able to form at the metal/nodule interface after some time.

6 FUTURE WORK

6.1 CHROMIA-FORMING ALLOYS

The observation made for A690 of the formation of a scale protective against both Cr-evaporation and oxidation should be explored further. Topics that could be investigated include:

- How different levels of alloying elements, mainly Cr, influence how this behaviour is triggered. By lowering the Cr content, a critical level of Cr-depletion would be reached more easily, although also the ability to form a secondary chromia scale would be impaired.
- Whether increased temperatures result in faster formation of a Ni-rich cap-layer due to higher Cr-evaporation rate. However, a higher temperature also results in more rapid diffusion of Cr in the metal.
- A more extensive characterisation of the oxide scale, in order to identify the exact phases formed and the elemental distribution, especially in cases where the Ni-rich cap-layer has formed.
- The use of longer exposure time, to see if a critical level of Cr-depletion is reached even under milder exposure conditions.
- A higher time resolution study of how the Ni-rich cap-layer is formed and evolves during long exposures.

6.2 ALUMINA-FORMING ALLOYS

This study shows that the addition of 1.3 wt.% Si results in a significant amount of Si appearing in the scale at 800 °C. However, the oxidation mechanism underling this phenomenon is not known. Further investigations that might shed light on this issue include:

- The use of more advanced microscopy, e.g., TEM examination of the scale formed on A197 when exposed to wet air, to identify the phases present, and an atom probe examination of the scale to determine how Si and Al are located in the scale.
- Computational simulations to determine the thermodynamic stabilities and kinetics of mullite and tridymite in alumina.
- In-situ SEM at 600 °C to investigate how the Fe-oxide nodules are formed and how they grow over time.

REFERENCES

1. *Global stainless steel production from 2005 to 2018*. Cited 2019-06-20; Available from: https://www.statista.com/statistics/223028/world-stainless-steel-production/.
2. Nilsson, J.O. *Can mankind survive without stainless steels*. 2014 Cited 2019-06-23; December 2014: Available from: http://www.stainless-steel-world.net/pdf/history_of_stainless_steel.pdf.
3. *Sources of Greenhouse Gas Emissions*. Cited 2019-06-23; Available from: https://www.epa.gov/ghgemissions/sources-greenhouse-gas-emissions.
4. Asteman, H., et al., *Indication of Chromium Oxide Hydroxide Evaporation During Oxidation of 304L at 873 K in the Presence of 10% Water Vapor.* Oxidation of Metals, 1999. **52**(1): p. 95-111.
5. Zhang, Z.G., et al., *Criteria for the formation of protective Al2O3 scales on Fe-Al and Fe-Cr-Al alloys.* Corrosion Science, 2006. **48**(3): p. 741-765.
6. Eklund, J., et al., *The influence of silicon on the corrosion properties of FeCrAl model alloys in oxidizing environments at 600 degrees C.* Corrosion Science, 2018. **144**: p. 266-276.
7. Bordenet, B., *Influence of novel cycle concepts on the high-temperature corrosion of power plants.* Materials and Corrosion-Werkstoffe Und Korrosion, 2008. **59**(5): p. 361-366.
8. Salmenoja, K., M. Hupa, and R. Backman, *Laboratory studies on the influence of gaseous HCl on superheater corrosion*. Impact of Mineral Impurities in Solid Fuel Combustion, ed. R.P. Gupta, T.F. Wall, and L. Baxter. 1999. 513-523.
9. Stanger, R., et al., *Oxyfuel combustion for CO2 capture in power plants.* International Journal of Greenhouse Gas Control, 2015. **40**: p. 55-125.
10. Pettersson, J., et al., *A pilot plant study of the effect of alkali salts on initial stages of the high temperature corrosion of alloy 304L*, in *High Temperature Corrosion and Protection of Materials 6, Prt 1 and 2, Proceedings*, P. Steinmetz, et al., Editors. 2004. p. 965-972.
11. Liu, K., C. Song, and V. Subramani, *Hydrogen and syngas production and purification technologies*. 2009: John Wiley & Sons.
12. Wang, Y., et al., *A review of polymer electrolyte membrane fuel cells: Technology, applications, and needs on fundamental research.* Applied Energy, 2011. **88**(4): p. 981-1007.
13. Stambouli, A.B. and E. Traversa, *Solid oxide fuel cells (SOFCs): a review of an environmentally clean and efficient source of energy.* Renewable & Sustainable Energy Reviews, 2002. **6**(5): p. 433-455.
14. Falk-Windisch, H., J.E. Svensson, and J. Froitzheim, *The effect of temperature on chromium vaporization and oxide scale growth on interconnect steels for Solid Oxide Fuel Cells.* Journal of Power Sources, 2015. **287**: p. 25-35.
15. Jiang, S.P. and X. Chen, *Chromium deposition and poisoning of cathodes of solid oxide fuel cells – A review.* International Journal of Hydrogen Energy, 2014. **39**(1): p. 505-531.
16. Aphale, A.N., et al., *Oxidation Behavior and Chromium Evaporation From Fe and Ni Base Alloys Under SOFC Systems Operation Conditions.* Jom, 2019. **71**(1): p. 116-123.
17. Kofstad, P., *High temperature corrosion.* Elsevier Applied Science Publishers, Crown House, Linton Road, Barking, Essex IG 11 8 JU, UK, 1988., 1988.
18. Young, D.J., *High temperature oxidation and corrosion of metals*. Vol. 1. 2008: Elsevier.
19. *The Ellingham diagram*. Cited 2019-09-05; Available from: https://doitpoms.ac.uk/tlplib/ellingham_diagrams/ellingham.php.
20. Birks, N., G.H. Meier, and F.S. Pettit, *Introduction to the high temperature oxidation of metals*. 2006: Cambridge University Press.
21. Wagner, C., *Beitrag zur theorie des anlaufvorgangs.* Zeitschrift für physikalische Chemie, 1933. **21**(1): p. 25-41.
22. Pujilaksono, B., et al., *Oxidation of Binary FeCr Alloys (Fe-2.25Cr, Fe-10Cr, Fe-18Cr and Fe-25Cr) in O-2 and in O-2 + H2O Environment at 600 degrees C.* Oxidation of Metals, 2011. **75**(3-4): p. 183-207.

23. Asteman, H., et al., *Influence of Water Vapor and Flow Rate on the High-Temperature Oxidation of 304L; Effect of Chromium Oxide Hydroxide Evaporation.* Oxidation of Metals, 2000. **54**(1): p. 11-26.
24. Huczkowski, P., et al., *Effect of gas flow rate on oxidation behaviour of alloy 625 in wet air in the temperature range 900–1000 °C.* Materials and Corrosion, 2017. **68**(2): p. 159-170.
25. Jones, D.A., *Principles and Prevention of Corrosion, 2nd.* Ed. Upper Saddle River, NY: Prentice Hall, 1996: p. 168-198.
26. Asteman, H., *Water Vapour induced active oxidation of stainless steel.* 2002.
27. Sutton, A.P., *Interfaces in crystalline materials.* Monographs on the Physice and Chemistry of Materials, 1995: p. 414-423.
28. Kofstad, P., *Nonstoichiometry, diffusion, and electrical conductivity in binary metal oxides.* 1972.
29. Nagai, H., S. Ishikawa, and K.-i. Shoji, *Electrical conductivity of sintered Cr2O3 with Fe2O3.* Transactions of the Japan Institute of Metals, 1985. **26**(1): p. 44-51.
30. Kofstad, P. and K. Lillerud, *On high temperature oxidation of chromium II. Properties of and the oxidation mechanism of chromium.* Journal of the electrochemical society, 1980. **127**(11): p. 2410-2419.
31. Lillerud, K. and P. Kofstad, *On high temperature oxidation of chromium I. Oxidation of annealed, thermally etched chromium at 800–1100 C.* Journal of the electrochemical society, 1980. **127**(11): p. 2397-2410.
32. Young, E.W.A., J.H. Gerretsen, and J.H.W. de Wit, *The Oxygen Partial Pressure Dependence of the Defect Structure of Chromium(III)Oxide.* Journal of The Electrochemical Society, 1987. **134**(9): p. 2257-2260.
33. Chen, G.F. and H.Y. Lou, *Predicting the oxide formation of Ni-Cr-Al alloys with nano-sized grain.* Materials Letters, 2000. **45**(5): p. 286-291.
34. Oishi, Y. and W. Kingery, *Self-diffusion of oxygen in single crystal and polycrystalline aluminum oxide.* The Journal of Chemical Physics, 1960. **33**(2): p. 480-486.
35. Heuer, A., *Oxygen and aluminum diffusion in α-Al2O3: how much do we really understand?* Journal of the European Ceramic Society, 2008. **28**(7): p. 1495-1507.
36. Naumenko, D., et al., *Correlation between the microstructure, growth mechanism, and growth kinetics of alumina scales on a FeCrAlY alloy.* Metallurgical and Materials Transactions a-Physical Metallurgy and Materials Science, 2007. **38A**(12): p. 2974-2983.
37. Sadique, S.E., et al., *High-Temperature Oxidation Behavior of Iron–Chromium–Aluminum Alloys.* Oxidation of Metals, 2000. **54**(5): p. 385-400.
38. Liu, F., et al., *TEM investigation of the oxide scales formed on a FeCrAlRE alloy (Kanthal AF) at 900 degrees C in dry O-2 and O-2 with 40% H2O.* Materials at High Temperatures, 2005. **22**(3-4): p. 521-526.
39. Schneider, H., J. Schreuer, and B. Hildmann, *Structure and properties of mullite - A review.* Journal of the European Ceramic Society, 2008. **28**(2): p. 329-344.
40. Young, D.J. and B.A. Pint, *Chromium volatilization rates from Cr 2 O 3 scales into flowing gases containing water vapor.* Oxidation of Metals, 2006. **66**(3-4): p. 137-153.
41. Holcomb, G.R., *Calculation of reactive-evaporation rates of chromia.* Oxidation of metals, 2008. **69**(3-4): p. 163-180.
42. Nickel, H., et al., *The effect of water vapor on the oxidation behavior of 9% Cr steels in simulated combustion gases.* Fresenius' journal of analytical chemistry, 1998. **361**(6-7): p. 540-544.
43. Casteel, M., et al., *Ionic Conductivity Method for measuring vaporized chromium species from solid oxide fuel cell interconnects.* International Journal of Hydrogen Energy, 2012. **37**(8): p. 6818-6829.
44. Bailey, J., *Volatile Cr contamination reduction in atmospheric pressure chemical vapor deposition systems by selective alloy oxidation.* Journal of the Electrochemical Society, 1997. **144**(10): p. 3568-3571.

45. Essuman, E., et al., *The effect of water vapor on selective oxidation of Fe-Cr alloys.* Oxidation of Metals, 2008. **69**(3-4): p. 143-162.
46. Ebbinghaus, B.B., *Thermodynamics of gas phase chromium species: The chromium oxides, the chromium oxyhydroxides, and volatility calculations in waste incineration processes.* Combustion and Flame, 1993. **93**(1): p. 119-137.
47. Opila, E.J., et al., *Theoretical and Experimental Investigation of the Thermochemistry of CrO2(OH)2(g).* The Journal of Physical Chemistry A, 2007. **111**(10): p. 1971-1980.
48. Panas, I., et al., *Chromic acid evaporation upon exposure of Cr2O3(S) to H2O(g) and O-2(g) - mechanism from first principles.* Chemical Physics Letters, 2004. **383**(5-6): p. 549-554.
49. Froitzheim, J., et al., *Investigation of Chromium Volatilization from FeCr Interconnects by a Denuder Technique.* Journal of The Electrochemical Society, 2010. **157**(9): p. B1295-B1300.
50. Tedmon, C., *The effect of oxide volatilization on the oxidation kinetics of Cr and Fe-Cr alloys.* Journal of the Electrochemical Society, 1966. **113**(8): p. 766-768.
51. Pujilaksono, B., et al., *Paralinear oxidation of chromium in O(2)+H(2)O environment at 600-700 degrees C.* Oxidation of Metals, 2008. **70**(3-4): p. 163-188.
52. Stanislowski, M., et al., *Chromium vaporization from high-temperature alloys I. Chromia-forming steels and the influence of outer oxide layers.* Journal of the Electrochemical Society, 2007. **154**(4): p. A295-A306.
53. Sachitanand, R., et al., *Evaluation of the oxidation and Cr evaporation properties of selected FeCr alloys used as SOFC interconnects.* International Journal of Hydrogen Energy, 2013. **38**(35): p. 15328-15334.
54. Froitzheim, J., et al., *Long term study of Cr evaporation and high temperature corrosion behaviour of Co coated ferritic steel for solid oxide fuel cell interconnects.* Journal of Power Sources, 2012. **220**: p. 217-227.
55. Trebbels, R., T. Markus, and L. Singheiser, *Investigation of Chromium Vaporization From Interconnector Steels With Spinel Coatings.* Journal of Fuel Cell Science and Technology, 2009. **7**(1): p. 011013-011013-6.
56. Stanislowski, M., et al., *Reduction of chromium vaporization from SOFC interconnectors by highly effective coatings.* Journal of Power Sources, 2007. **164**(2): p. 578-589.
57. Essuman, E., et al., *Enhanced internal oxidation as trigger for breakaway oxidation of Fe–Cr alloys in gases containing water vapor.* Scripta Materialia, 2007. **57**(9): p. 845-848.
58. Rahmel, A. and J. Tobolski, *Einfluss von wasserdampf und kohlendioxyd auf die oxydation von eisen in sauerstoff bei hohen temperaturen.* Corrosion Science, 1965. **5**(5): p. 333-346.
59. Henry, S., et al., *Characterization of Chromia Scales Grown on Pure Chromium in Different Oxidizing Atmospheres.* Materials at High Temperatures, 2000. **17**(2): p. 231-234.
60. Opila, E.J., et al., *Predicting oxide stability in high-temperature water vapor.* Jom, 2006. **58**(1): p. 22-28.
61. Bhowmick, S., et al., *ASSESSMENT OF CHROMIUM EVAPORATION FROM CHROMIA AND ALUMINA FORMING ALLOYS*, in *Advances in Solid Oxide Fuel Cells Vii*, N.P. Bansal, et al., Editors. 2011. p. 115-124.
62. Stanislowski, M., et al., *Chromium vaporization from alumina-forming and aluminized alloys.* Solid State Ionics, 2008. **179**(40): p. 2406-2415.
63. Götlind, H., et al., *The Effect of Water Vapor on the Initial Stages of Oxidation of the FeCrAl Alloy Kanthal AF at 900 °C.* Oxidation of Metals, 2007. **67**(5): p. 251-266.
64. States, S.S.I.o.t.U., et al., *Design Guidelines for the Selection and Use of Stainless Steel*. 1993: Specialty Steel Industry of the United States.
65. Rebak, R., *Crystallinne alloys: nickel*. 2013. 197-218.
66. Kim, I.S., et al., *Effect of microstructural characteristics on the low cycle fatigue behaviors of cast Ni-base superalloys.* Materials Characterization, 2015. **106**: p. 375-381.
67. Pike, L. *Development of a fabricable gamma-prime (γ') strengthened superalloy*. in *Proceedings of The 11th International Symposium on Superalloys*. 2008.

68. Pint, B.A., J. Leibowitz, and J.H. DeVan, *The effect of an oxide dispersion on the critical Al content in Fe-Al alloys.* Oxidation of Metals, 1999. **51**(1-2): p. 181-197.
69. Stott, F.H., G.C. Wood, and J. Stringer, *THE INFLUENCE OF ALLOYING ELEMENTS ON THE DEVELOPMENT AND MAINTENANCE OF PROTECTIVE SCALES.* Oxidation of Metals, 1995. **44**(1-2): p. 113-145.
70. Tomaszewicz, P. and G.R. Wallwork, *OBSERVATIONS OF NODULE GROWTH DURING THE OXIDATION OF PURE BINARY IRON ALUMINUM-ALLOYS.* Oxidation of Metals, 1983. **19**(5-6): p. 165-185.
71. Tomaszewicz, P. and G.R. Wallwork, *THE OXIDATION OF HIGH-PURITY IRON-CHROMIUM-ALUMINUM ALLOYS AT 800-DEGREES-C.* Oxidation of Metals, 1983. **20**(3-4): p. 75-109.
72. Boggs, W.E., *OXIDATION OF IRON-ALUMINUM ALLOYS FROM 450 DEGREES TO 900 DEGREES C.* Journal of the Electrochemical Society, 1971. **118**(6): p. 906-&.
73. Grobner, P.J., *The 885° f (475° c) embrittlement of ferritic stainless steels.* Metallurgical Transactions, 1973. **4**(1): p. 251-260.
74. Spear, W.S. and D.H. Polonis, *INTERSTITIAL PRECIPITATION IN FE-CR-AL ALLOYS.* Metallurgical and Materials Transactions a-Physical Metallurgy and Materials Science, 1994. **25**(6): p. 1135-1146.
75. Ejenstam, J., et al., *Microstructural stability of Fe-Cr-Al alloys at 450-550 degrees C.* Journal of Nuclear Materials, 2015. **457**: p. 291-297.
76. Lim, J., I.S. Hwang, and J.H. Kim, *Design of alumina forming FeCrAl steels for lead or lead–bismuth cooled fast reactors.* Journal of Nuclear Materials, 2013. **441**(1): p. 650-660.
77. Guan, S.W., J. Corkum, and W. Smeltzer, *OXIDATION BEHAVIOR OF FE-AL-SI ALLOYS AT 1073-K AND 1173-K*. High Temperature Corrosion of Advanced Materials and Protective Coatings, ed. Y. Saito, B. Onay, and T. Maruyama. 1992. 75-82.
78. Rahmel, A. and M. Schutze, *MECHANICAL ASPECTS OF THE RARE-EARTH EFFECT.* Oxidation of Metals, 1992. **38**(3-4): p. 255-266.
79. Whittle, D.P. and J. Stringer, *IMPROVEMENTS IN HIGH-TEMPERATURE OXIDATION RESISTANCE BY ADDITIONS OF REACTIVE ELEMENTS OR OXIDE DISPERSIONS.* Philosophical Transactions of the Royal Society a-Mathematical Physical and Engineering Sciences, 1980. **295**(1413): p. 309-+.
80. Tolpygo, V.K. and H.J. Grabke, *The effect of impurities on the alumina scale growth: An alternative view.* Scripta Materialia, 1997. **38**(1): p. 123-129.
81. Mortazavi, N., et al., *Interplay of water and reactive elements in oxidation of alumina-forming alloys.* Nature Materials, 2018. **17**(7): p. 610-+.
82. Orloff, J., M. Utlaut, and L. Swanson, *Applications of focused ion beams*, in *High Resolution Focused Ion Beams: FIB and its Applications*. 2003, Springer. p. 205-290.
83. Fournier-Salaün, M.-C. and P. Salaün, *Quantitative determination of hexavalent chromium in aqueous solutions by UV-Vis spectrophotometer.* Central European Journal of Chemistry, 2007. **5**(4): p. 1084-1093.
84. Goldstein, J.I., et al., *Scanning electron microscopy and X-ray microanalysis*. 2017: Springer.
85. Williams, D.B. and C.B. Carter, *The Transmission Electron Microscope*, in *Transmission Electron Microscopy: A Textbook for Materials Science*. 1996, Springer US: Boston, MA. p. 3-17.
86. Bluhm, H., *4 - X-ray photoelectron spectroscopy (XPS) for in situ characterization of thin film growth*, in *In Situ Characterization of Thin Film Growth*, G. Koster and G. Rijnders, Editors. 2011, Woodhead Publishing. p. 75-98.
87. Xiao, J., et al., *Influence of humidity on high temperature oxidation of Inconel 600 alloy: Oxide layers and residual stress study.* Applied Surface Science, 2013. **284**: p. 446-452.
88. Asteman, H., J.E. Svensson, and L.G. Johansson, *Effect of water-vapor-induced Cr vaporization on the oxidation of austenitic stainless steels at 700 and 900 degrees C - Influence of Cr/Fe ratio in alloy and Ce additions.* Journal of the Electrochemical Society, 2004. **151**(3): p. B141-B150.

89. Gotlind, H., et al., *The effect of water vapor on the initial stages of oxidation of the FeCrAl alloy Kanthal AF at 900 degrees C.* Oxidation of Metals, 2007. **67**(5-6): p. 251-266.
90. Alnegren, P., et al., *Temperature dependence of corrosion of ferritic stainless steel in dual atmosphere at 600-800 degrees C.* Journal of Power Sources, 2018. **392**: p. 129-138.